

24 Email: Wei-Kuo.Tao-1@nasa.gov

25

26 **Key Points**

- 27
- A new 4ICE microphysics scheme is implemented in a regional scale model.
- 28
- Radar reflectivities and rainfall intensities are sensitive to microphysics scheme.
- 29
- The 4ICE scheme shows improvements over 3ICE schemes with either
- 30 graupel or hail alone.

31

32 **Abstract**

33 The Goddard microphysics scheme was recently improved by adding a 4th ice class
34 (frozen drops/hail). This new 4ICE scheme was implemented and tested in the Goddard
35 Cumulus Ensemble model (GCE) for an intense continental squall line and a moderate,
36 less-organized continental case. Simulated peak radar reflectivity profiles were improved
37 both in intensity and shape for both cases as were the overall reflectivity probability
38 distributions versus observations. In this study, the new Goddard 4ICE scheme is
39 implemented into the regional-scale NASA Unified - Weather Research and Forecasting
40 model (NU-WRF) and tested on an intense mesoscale convective system that occurred
41 during the Midlatitude Continental Convective Clouds Experiment (MC3E). The NU-
42 WRF simulated radar reflectivities, rainfall intensities, and vertical and horizontal
43 structure using the new 4ICE scheme agree as well as or significantly better with
44 observations than when using previous versions of the Goddard 3ICE (graupel or hail)
45 schemes. In the 4ICE scheme, the bin microphysics-based rain evaporation correction
46 produces more erect convective cores, while modification of the unrealistic collection of
47 ice by dry hail produces narrow and intense cores, allowing more slow-falling snow to be
48 transported rearward. Together with a revised snow size mapping, the 4ICE scheme
49 produces a more horizontally stratified trailing stratiform region with a broad, more
50 coherent light rain area. In addition, the NU-WRF 4ICE simulated radar reflectivity
51 distributions are consistent with and generally superior to those using the GCE due to the
52 less restrictive open lateral boundaries.

53

54 Key words

55 Ice Microphysics, Severe rainfall, WRF

56

57

58

59 **1. Introduction**

60 Many new and improved microphysical parameterization schemes have been
61 developed over the past few decades [e.g., *Ferrier, 1994; Meyers et al., 1997; Reisner et*
62 *al., 1998; Hong et al., 2004; Walko et al., 1995; Colle et al., 2004; Zhu and Zhang, 2004;*
63 *Morrison et al., 2005; Straka and Mansell, 2005; Milbrandt and Yau, 2005; Morrison*
64 *and Grabowski, 2008; Thompson et al., 2004, 2008; Dudhia et al., 2008, Morrison and*
65 *Milbrandt, 2014, 2015; Morrison et al., 2015; and many others]. Please see *Levin and*
66 *Cotton [2008]* and *Tao and Moncrieff [2009]* for a review of the microphysics used in
67 cloud-resolving models. In addition, please see Table 1 in *Tao et al. [2011a]* and *Lang et*
68 *al. [2014]* for a brief review of microphysics parameterizations. They include one- and
69 two-moment bulk schemes with two or more ice classes, three-moment bulk schemes,
70 and spectral bin microphysics schemes. Different approaches have been used to examine
71 the performance of new schemes. One approach is to examine the sensitivity of
72 precipitation processes to different microphysical schemes. This approach can help to
73 identify the strength(s) and/or weakness(es) of each scheme in an effort to improve their
74 overall performance [e.g., *Ferrier et al., 1995; Straka and Mansell, 2005; Milbrandt and*
75 *Yau, 2005*]. Idealized simulations have also been used to test new microphysical
76 schemes by showing their behavior in a setting that is open to simpler interpretation. In
77 addition, another approach has been to examine specific microphysical processes (e.g.,
78 turning melting/evaporation on or off, reducing the auto-conversion rate from cloud water
79 to rain, etc.) within one particular microphysical scheme. This approach can help to
80 identify the dominant microphysical processes within a particular scheme (i.e.,
81 evaporation, melting of large precipitating ice particles, etc.) responsible for determining*

82 the organization and structure of convective systems [e.g., *Tao et al.*, 1995; *Wang*, 2002;
83 *Colle et al.*, 2005; *Zhu and Zhang*, 2006a; and many others]. Table 1 lists the major
84 characteristics for a range of previously published modeling papers in terms of model
85 used, microphysics schemes (number of ice classes, number of moments), model
86 resolution, integration time and case(s). This paper will apply the first approach to
87 examine the performance of several different Goddard microphysical schemes.

88 Cloud-resolving models (CRMs) are typically run at horizontal grid spacing on
89 the order of 1-2 km or finer and can simulate the dynamical and microphysical processes
90 associated with deep, precipitating atmospheric convection. One advantage of using
91 CRMs is that it allows for explicit interactions between cloud-microphysics, radiation and
92 surface processes. Another advantage is that each model grid is either fully clear or
93 cloudy, so that no cloud (maximum, random) overlap assumption is required.

94 Simulations using the Goddard Cumulus Ensemble (GCE) model with a new
95 4ICE (cloud ice, snow, graupel and hail) scheme for an intense squall line observed over
96 central OK during the Midlatitude Continental Convective Clouds Experiment (MC3E)
97 and loosely organized moderate convection observed over Amazonia during the Tropical
98 Rainfall Measuring Mission Large-Scale Biosphere-Atmosphere Experiment in
99 Amazonia (TRMM LBA) [*Lang et al.*, 2014] produced peak reflectivity profiles that
100 were superior to previous iterations of the Goddard 3ICE graupel microphysics scheme
101 [*Tao et al.*, 2003; *Lang et al.*, 2007, 2011] with peak intensities closer to the observed and
102 that monotonically decreased with height also as observed. The 4ICE scheme was able to
103 match the infrequent but relatively rare occurrence of intense echoes within the
104 convective cores. Simulated reflectivity distributions versus height were also improved

105 versus radar in both cases compared to the earlier 3ICE versions. The main reason for
106 developing the 4ICE scheme was to expand the ability of the microphysics to include
107 more intense convection without the need to switch schemes (i.e., from 3ICE-graupel to
108 3ICE-hail) *a priori*. Furthermore, hail and graupel can occur in real weather events
109 simultaneously. Therefore, a 4ICE scheme (cloud ice, snow, graupel and hail) is useful
110 for numerical weather prediction, especially for high-resolution prediction of severe local
111 thunderstorms, mid-latitude squall lines and tornadoes. Current and future global high-
112 resolution CRMs need the ability to predict/simulate a variety of weather systems from
113 weak to intense (i.e., tropical cyclones, thunderstorms) over the entire globe; a 4ICE
114 scheme can respond appropriately to such a variety of environmental conditions.

115 GCE model simulations are typically forced with the observed large-scale
116 advective tendencies for temperature and water vapor using cyclic lateral boundary
117 conditions [i.e., *Tao et al.*, 2003; *Moncrieff et al.*, 1996] as was the case for the
118 simulations of the intense MC3E squall line in *Lang et al.* [2014]. The horizontally
119 uniform forcing and cyclic boundaries can influence the simulated spatial structures of
120 the squall line. Therefore, the performance of the 4ICE scheme needs to be further
121 assessed with different types of numerical models and initial/lateral boundary conditions.
122 Improved versions of the Goddard bulk microphysics with different options (3ICE and
123 4ICE) have been implemented into the NASA Unified - Weather Research and
124 Forecasting model (NU-WRF). The major objective of this study is to examine the
125 performance of these different Goddard schemes in terms of precipitation processes,
126 rainfall (including its intensity), the vertical distribution of cloud species, and in
127 comparison with observed radar profiles. Data collected during the joint NASA/DOE

128 MC3E field campaign will be used for this study. The paper has the following
129 organization. Section 2 describes NU-WRF, changes to the Goddard microphysics, the
130 MC3E case, and the numerical experiments. Section 3 presents the simulation results and
131 their evaluation versus observations, and the summary and conclusions are given in
132 section 4.

133

134 **2. Model description**

135 *2.1 NU-WRF*

136 Recently, several physical process parameterizations developed for NASA have
137 been implemented into WRF to better represent/simulate cloud-aerosol-precipitation-land
138 surface processes and interactions on satellite-resolvable scales (~1 km grid spacing).
139 These parameterizations have been implemented into several WRF versions from 3.1.1
140 up through 3.5.1, collectively known as the NASA Unified - WRF or NU-WRF [*Peters-*
141 *Lidard et al., 2014*]. NU-WRF is available to non-NASA users. Several NASA physical
142 packages (microphysics, radiation) have also been implemented into the NCAR ARW
143 (Advanced Research WRF). These physical processes include CRM-based microphysics
144 and radiation [*Tao et al., 2003; Lang et al., 2007, 2011, 2014*] that have been tested on
145 convective systems in different environments, including a linear convective system in
146 Oklahoma from the International H2O project (IHOP-2002) [*Santanello et al., 2009*], an
147 Atlantic hurricane (Hurricane Katrina from 2005) [*Tao et al., 2011a*], high latitude snow
148 events from the Canadian CloudSat CALIPSO Validation Project (C3VP) in 2007 [*Shi et*
149 *al., 2010; Iguchi et al., 2012a,b, 2014*], a Pacific typhoon [Typhoon Morakot, 2009; *Tao*
150 *et al. 2011b*], and mesoscale convective systems (MCSs) in Africa [*Shi et al., 2013*] and

151 the Southern Great Plains (MC3E in 2011 [*Tao et al.*, 2013]). In addition, two other
152 major NASA modeling components have been coupled with NU-WRF representing land
153 surfaces (i.e., the Land Information System (LIS) [*Kumar et al.*, 2007]) and aerosols (i.e.,
154 the WRF Chemistry Model and Goddard Chemistry Aerosol Radiation and Transport
155 Model (GOCART) [*Chin et al.*, 2000, 2002, 2004]).

156

157 2.2 *Goddard microphysics schemes*

158 Several versions of the Goddard microphysics schemes have been implemented into NU-
159 WRF. These schemes include the 3ICE scheme with graupel [*Tao and Simpson*, 1989,
160 1993; *Lang et al.*, 2007, 2011], the 3ICE scheme with hail [*McCumber et al.*, 1991; *Tao*
161 *et al.*, 2003], and the new 4ICE scheme with both graupel and hail [*Lang et al.*, 2014].
162 Please see the Appendix for the details on these schemes as well as for the several further
163 enhancements that have been made to the 4ICE scheme that were incorporated in this
164 study.

165

166 2.3 *Case*

167 MC3E was a joint field campaign between the DOE ARM Climate Research
168 Facility and NASA's Global Precipitation Measurement (GPM) mission Ground
169 Validation (GV) program [*Petersen et al.*, 2009]. It took place in central Oklahoma from
170 22 April to 6 June 2011. Some of its major objectives involve the use of high-resolution
171 CRMs in precipitation science and include: (1) testing the fidelity of CRM simulations
172 via intensive statistical comparisons between simulated and observed cloud properties
173 and latent heating (LH) fields for a variety of case types, (2) establishing the limits of

174 CRM space-time integration capabilities for quantitative precipitation estimates, and (3)
175 supporting the development and refinement of physically-based GPM microwave imager
176 (GMI), dual-frequency precipitation radar (DPR), and DPR-GMI combined retrieval
177 algorithms using ground-based observations, aircraft measurements, airborne radar and
178 radiometer, and CRM simulations. The focus of this study will be the intense squall line
179 case presented in *Lang et al.* [2014].

180 On 20 May 2011 a deep, upper-level low over the central Great Basin moved
181 across the central and southern Rockies and into the central and northern Plains. A
182 surface low pressure center in southeastern Colorado drew warm, moist air from the
183 southern Plains to a warm front over Kansas, while a dry line extended southward from
184 the Texas/Oklahoma Panhandle. As a result, several convective lines formed over the
185 Great Plains and propagated eastward. The northern portion of a long convective line
186 began to enter the MC3E sounding network around 07 UTC 20 May and by 09 UTC had
187 merged with ongoing convection near the KS-OK border to form a more intense
188 convective segment with a well-defined trailing stratiform region that then propagated
189 through the network between 09 and 12 UTC. The convection along the leading edge of
190 this intense squall line exited the network around 13 UTC leaving behind a large area of
191 stratiform rain. For further details see *Lang et al.* [2014]. This case was also simulated
192 with NU-WRF by *Tao et al.* [2013], but the focus was on the diurnal variation of
193 precipitation.

194

195 2.4 *Model set-up*

196 Figure 1 shows the model grid configuration, which includes an outer domain and
197 two inner-nested domains, having 9-, 3- and 1-km horizontal grid spacings with
198 $524 \times 380 \times 61$, $673 \times 442 \times 61$, $790 \times 535 \times 61$ grid points, respectively. Time steps of 18, 6
199 and 2 seconds were used in these nested grids, respectively. The Grell-Devenyi cumulus
200 parameterization scheme [Grell and Devenyi, 2002] was used for the outer grid (9 km)
201 only. For the inner two domains (3- and 1-km), the convective scheme was turned off.
202 The PBL parameterization employed the Mellor-Yamada-Janjic [Mellor and Yamada,
203 1992] Level-2 turbulence closure model through the full range of atmospheric turbulent
204 regimes. The scheme was coded/modified by Dr. Janjic for the NCEP Eta model.

205 The Goddard broadband two-stream (upward and downward fluxes) approach
206 was used for the short- and long-wave radiative flux and atmospheric heating calculations
207 [Chou and Suarez, 1999, 2001] and its explicit interactions with clouds (microphysics).
208 Model terrain is smoothed from the 5-m (~5-km), 2-m (~4-km) and 30-second (~0.9 km)
209 USGS terrain database for the three nested domains, respectively. Simulations start at 00
210 UTC 20 May 2014 for 48 hours of model integration. Initial conditions are from the
211 GFS-FNL (Global Forecast System Final global gridded analysis [archive](#)) as are the
212 lateral boundary conditions, which are updated every 6 hours.

213

214 2.5 Numerical experiments

215 Three numerical experiments are conducted for the MC3E case using various
216 versions of the Goddard microphysics schemes: 3ICE-graupel [Lang *et al.*, 2011] termed
217 “Graupel,” 3ICE-hail [McCumber *et al.* 1990; Tao *et al.* 2003] termed “Hail,” and the

218 new 4ICE scheme [Lang et al. 2014] with additional modifications termed “4ICE”.
219 Table 2 shows the list of numerical experiments performed for this case.

220

221 **3. Results**

222 *3.1 Surface rainfall and its convective and stratiform characteristics*

223 The National Mosaic and Multi-Sensor QPE (NMQ) system is a multiradar,
224 multisensor system, ingesting base-level data from all available radars (NEXRAD,
225 Canadian Radar, TDWR, gap radars) at any given time, performs quality control, and
226 then combines reflectivity observations from individual radars onto a unified 3D
227 Cartesian frame. Surface rainfall observation is from next generation quantitative
228 precipitation estimation (Q2) radar-only product, which is a key component in NMQ
229 system. Both their radar and precipitation data have a spatial and temporal resolution of
230 1 km and 5 min, respectively [Zhang et al., 2011].

231 The NU-WRF simulated rainfall for the three different Goddard microphysical
232 schemes at 10 UTC on 20 May 2014 is shown in Fig. 2. All three NU-WRF simulations
233 have a smaller light rain area in the stratiform region than was observed, though the
234 combined coherence and intensity of the 4ICE simulation appears closer to the observed
235 at the time shown (typical of other times). The observed convective system is a fast-
236 propagating system. This feature is also generally captured by all three of the NU-WRF
237 simulations (not shown). There are some notable differences between the simulations,
238 however, which are well illustrated in Fig. 2. For the Graupel scheme, the area of heavy
239 rainfall at the leading edge of the system appears smallest and narrowest. Though the
240 Graupel scheme produces a broader, more coherent area of light to moderate rainfall than

241 the Hail scheme, such extensive areas of moderately intense rain were not observed. The
242 areas of heavy rainfall in the Hail simulation are more robust than in the Graupel
243 simulation but lack the coherent extended arc structure of the observations, the 4ICE
244 scheme, and to some degree the Graupel scheme. The Hail scheme produces a smaller,
245 less coherent light rain area than the other two schemes, but its intensity appears similar
246 to that observed. In terms of the rainfall pattern, the 4ICE scheme agrees better overall
247 with the observations than the other two simulations, with a convective leading edge that
248 is more intense than the Graupel simulation and also longer and more coherent than the
249 Hail simulation. The 4ICE trailing stratiform region also appears to match better with the
250 observations, being deeper and more coherent than in the Hail simulation but remaining
251 more uniform and not overly intense as in the Graupel simulation. Without hail, too
252 much moderate-falling graupel is transported rearward in the Graupel simulation and
253 does not fall out in the convective leading edge, whereas with the hail scheme, “dry
254 collection” causes more of the slow-falling snow to be collected and fall out as hail in the
255 convective leading edge. The 4ICE scheme modulates these biases by allowing only ice
256 that was formed in a manner that would produce high particle density (e.g., freezing
257 drops or extreme riming) to fall out as hail in the convective leading edge and therefore
258 more slow-falling snow to be transported rearward to maintain a broader, more uniform
259 light rain area.

260 Rainfall can also be separated into convective and stratiform regions. There are
261 several reasons for making this distinction [Houze, 1997]. For example, precipitation
262 rates are generally much higher in the convective region. Ice particles tend to be rimed in
263 the convective region and to be aggregates in the stratiform region. Microphysics and, as

264 a consequence, surface rainfall and the vertical distribution of latent heating are also
265 found to be different in these two regions [see the reviews by Houze, 1997 and Tao,
266 2003]. The convective-stratiform partitioning method used in this study is based on the
267 horizontal radar reflectivity gradient [Steiner et al., 1995]. The criteria for identifying the
268 convective region are based on intensity, “peakedness”, and the surrounding area as
269 described by Steiner et al. [1995]. Because that scheme was originally developed for
270 tropical convection, several input parameters for the partitioning scheme were tuned to fit
271 mid-latitude scenarios [Feng et al., 2011]. A 2-km mean sea level (MSL) height (versus
272 3 km in Steiner et al. [1995]) is used as the analysis level in order to avoid bright band
273 contamination, and the reflectivity threshold for the convective region is set to 43 dBZ
274 (40 dBZ in Steiner et al. [1995]), according to the Z-R relationship in mid-latitudes. The
275 rest of the echoes that exceed 10 dBZ, but are not identified as convective core, are
276 designated as stratiform rain region [Feng et al., 2011] (See also *Lang et al.* [2004] for a
277 review of convective and stratiform observational studies, modeling studies and different
278 convective–stratiform separation methods.). The same convective-stratiform separation
279 method is used for both the observations and model results.

280 Figure 3 illustrates typical similarities and differences between the observed and
281 simulated convective and stratiform areas. As expected the convective regions in all
282 three simulations (Figure 3b-d) are located at the leading edge of the convective system,
283 consistent with NEXRAD data (Figure 3a; see section 3.3). The Graupel and 4ICE
284 simulations produce a broad arc shape similar to that observed; the Hail scheme,
285 however, only produces a small arc-shaped convective region over southern OK. All
286 three simulations underestimate the stratiform rain area, though in terms of character, the

287 4ICE simulation is closest to the observations.

288 Tables 3 and 4 show the rainfall amount and area coverage quantitatively (at 1-km
289 grid spacing) obtained from 06 UTC to 12 UTC on 20 May 2011. Data from the first 6
290 hours were not used since the simulations use a cold start. Both the modeled and
291 observed convective systems are propagating squall lines, though the simulated
292 convective lines propagate faster than observed and move out of the inner domain after
293 12 UTC. Only areas with rain rates greater than 0.15 mm/h, which is based on the Q2
294 minimum detectable rain rate, are partitioned. In the simulations, light rain regions (e.g.
295 shallow cumulus or elevated anvil) that are not classified as either convective or
296 stratiform region contribute to totals larger than the sum of the convective and stratiform
297 parts. In addition, the partition scheme, which relies on 3D output, is applied every 10
298 min rather than every time step as in total accumulations. The results show that the
299 rainfall amount in the 4ICE run is about 10% more than in the 3ICE runs (both Graupel
300 and Hail), closest to that observed; however, its total rainfall is still underestimated by
301 about 27% (Table 3). The model results from the previous study [Tao *et al.* 2013] also
302 underestimated the total rainfall amount by about 26% (with 2-km grid spacing in the
303 inner domain). Tao *et al.* [2013] conducted sensitivity tests on the surface processes and
304 terrain height, but those did not result in an increase in total rainfall amount. Neither the
305 improved microphysics nor the finer resolutions have much impact on the total amount
306 rainfall. This underestimation is also shown in the runs with other WRF microphysics
307 schemes (Part II) and sensitivity tests on surface fluxes and terrain height [Tao *et al.*
308 2013]. Initiating the model with clear skies (i.e., a cold start), the initial or boundary
309 conditions, and the fact that the observed line extended farther south than the inner-most

310 domain could all be factors, but further study is needed to identify the reason(s) for this
311 deficiency in the rainfall amount. The model simulated total rain coverage for all three
312 simulations is also underestimated (Table 4) as the simulations fail to capture the
313 complete extent of the observed stratiform rain area over western OK. This could be due
314 to the real squall line extending further south than in the simulations, thereby boosting the
315 development of the stratiform region at the southern end of the analysis domain relative
316 to the simulations.

317 Tables 3 and 4 also show the observed and simulated rainfall amounts and area
318 coverage in the convective and stratiform regions. All three simulations reproduce
319 observed convective area coverage to within a factor of 0.8-1.2 times that observed, but
320 all simulations also underestimate total convective rainfall by a factor of 0.3-0.5 or more;
321 thus the simulated convective rain rates are weaker than observed on average. All three
322 simulations also underestimate stratiform area coverage by a factor of roughly 0.4 while
323 underestimating stratiform rainfall by a factor of 0-0.35; thus simulated stratiform rain
324 rates tend to be more intense than observed. The Graupel simulation produces the most
325 stratiform rain (~5 mm) and area (~15%); although rainfall amount is close to that
326 observed, it is distributed over an appreciably smaller area than observed, indicating that
327 typical stratiform rain rates are too intense. Consistent with previous modeling results,
328 the Hail scheme produces less stratiform but more convective rain than the Graupel
329 scheme. For example, McCumber *et al.* [1991] suggested that the most important
330 characteristic difference between graupel and hail is the terminal velocity. For graupel, a
331 smaller terminal velocity allows it to enter the stratiform (or behind the convective)
332 region, where it becomes an important constituent of the stratiform region. The 4ICE

333 scheme produces roughly 30% more stratiform rainfall than the Hail scheme over roughly
334 a 10% larger stratiform area, indicating that its overall stratiform rain is more intense.
335 Stratiform rainfall accounts for about 53%, 35% and 39 % of the total rainfall in the
336 Graupel, Hail and 4ICE schemes, respectively (Table 3). The Hail scheme yields a
337 stratiform rain percentage of 35% in closest agreement with the observations but with
338 rates and coverage that differ substantially from those observed; the 4ICE scheme
339 stratiform rain percentage is only slightly higher, with similar biases. The 4ICE scheme
340 has more convective rain in better agreement with the observations because it has a
341 longer convective region owing to being better organized than the Hail scheme.

342 Figure 4a shows PDFs of the simulated and observed surface rainfall intensity.
343 Both the 4ICE and Hail schemes have a higher proportion of heavy precipitation (i.e., >
344 30-40 mm/h) than the Graupel scheme. This is because larger hail falls quickly before
345 melting to form large raindrops (and consequently high rain intensities). This result is in
346 better agreement with observations than the Graupel scheme. In addition, the 4ICE and
347 Hail schemes produce less moderate precipitation (i.e., 10-20 mm/h) than the Graupel
348 scheme, which is also in better agreement with observations. However, the two schemes
349 with hail still simulated less very heavy rainfall (i.e., > 40-50 mm/h) than was observed,
350 though they are far superior to the Graupel scheme in this regard. Despite high temporal
351 and spatial resolution, radar-only Q2 rainfall has its own limitations. As discussed in
352 Tang et al. [2012], daily averaged rainfall from Q2 has a positive bias compared to
353 gauge-corrected Stage IV and the NCEP Climate Prediction Center (CPC) rain gauge
354 estimates during summer (JJA, 2010). However, it is uncertain as to how much of the
355 positive bias is contributed from those grids with very heavy rain rates. The Hail scheme,

356 which has no graupel, generally simulated slightly more intense rainfall than the 4ICE
357 scheme. The Graupel scheme generally produced more lighter and less intense
358 precipitation (i.e., < 20-30 mm/h) compared to the Hail and 4ICE schemes as moderate-
359 falling graupel is the dominant cloud species in the Graupel scheme. Rainfall PDFs for
360 the convective region (Fig. 4b) are much flatter than the total but with similar biases; the
361 Hail and 4ICE schemes are comparable to one another and somewhat underestimate the
362 occurrence of rain rates above 40 mm/h whereas the Graupel scheme greatly
363 underestimates their occurrence. Rainfall PDFs for the stratiform region (Fig. 4c) are
364 much steeper than the convective. Overall, the Hail and 4ICE PDFs tend to agree well
365 with the observed, having similar slopes while the Graupel rainfall PDF appears too
366 steep, overestimating rates between 10 to 20 mm/h and underestimating those above 30
367 mm/h. The simulated rainfall intensity (heavy or light rainfall) can be important for
368 hydrology and surface processes (e.g., hydrological as well as ocean mixed layer
369 models).

370

371 3.2 *Hydrometeor properties*

372 Figure 5 shows vertical profiles of the horizontal domain- and time-averaged
373 cloud species (i.e., cloud water, rain, cloud ice, snow, graupel and hail). The low-level
374 rain and cloud water mixing ratios show little variation between the three schemes.
375 Cloud ice, snow and graupel are dominant cloud species in the Graupel scheme (Figure
376 5a). The large snow and graupel amounts in the Graupel scheme lead to more moderate
377 melting over a larger area and thus a large average rain mixing ratio immediately beneath
378 the melting layer. The Graupel scheme produced a much larger graupel profile compared

379 to the 4ICE scheme, as both rimed particles and frozen drops are treated as graupel,
380 which has a moderate fall speed and remains suspended much longer than hail. Hail has
381 the fastest fall speeds, allowing it to fall further into the lower troposphere before fully
382 melting as clearly shown in both the Hail and 4ICE schemes (Figures 5b and c). As in
383 the Graupel scheme, snow is also a dominant cloud species in the Hail and 4ICE
384 schemes. One major difference is that the Hail scheme has very little cloud ice compared
385 to the Graupel and 4ICE schemes. The vertical distribution of snow and hail for the Hail
386 scheme is quite similar to the results of Lin *et al.* [1983], which are also for a midlatitude
387 thunderstorm, as it is mainly based on Lin *et al.* [1983].

388 Table 5 shows the domain- (vertical and horizontal) and time-averaged amounts
389 of cloud species. The most abundant cloud species are cloud ice, snow and graupel in the
390 Graupel scheme. Snow is the most abundant cloud specie in the Hail scheme, which also
391 had very little cloud ice compared to the other two schemes. The Graupel scheme
392 produced more cloud ice and snow than did the Hail scheme, as in earlier GCE model
393 simulations [cf. *McCumber et al.*, 1991; *Lang et al.*, 2007, 2011]. For the 4ICE scheme,
394 snow and cloud ice are the most abundant ice species. The Hail scheme has slightly more
395 hail than the 4ICE scheme, which allows for graupel formation. All of the schemes
396 simulated similar amounts of cloud water, rain, and total rainfall.

397 An accurate vertical distribution of cloud species is important for satellite
398 retrievals [i.e., *Lang et al.*, 2007; *Olson et al.*, 2006]. Unrealistic precipitation ice
399 contents (i.e., snow and graupel), for example, can bias the simulated brightness
400 temperatures and make it difficult to infer cloud properties from remote sensing data,
401 which link them with synthetic values from models [*Matsui et al.*, 2013].

402 Microphysics schemes vary in their representation of cloud processes, leading to
403 differing amounts of hydrometeor types. Tables 6, 7 and 8 show the cloud species in the
404 convective, stratiform, and cloudy (but not convective or stratiform) regions for the three
405 Goddard schemes. For the Graupel scheme, snow and graupel are the most abundant
406 hydrometeors in the both the convective and stratiform regions. The Hail scheme also
407 has a relatively large amount of snow in both the convective and stratiform region, but
408 the amounts are less than for the Graupel scheme. The Hail scheme has the largest
409 amount of hail in the convective region. The large size and faster fall speed of hail
410 causes it to melt at significantly lower levels than graupel, and the higher convective rain
411 rate in the Hail simulation is mainly due to the presence of hail. The Hail scheme
412 produces significantly less total precipitating ice and less rainfall than the Graupel and
413 4ICE schemes in the stratiform region. This is consistent with the rainfall amounts and
414 stratiform percentages shown in Table 3. For the 4ICE scheme, the snow mass is also
415 larger in the convective and stratiform regions compared to other cloud species but
416 especially in the stratiform region. The Graupel scheme has more total precipitating ice
417 (snow and graupel) than either the 4ICE (snow, graupel and hail) or Hail scheme in the
418 stratiform region (Table 7), explaining its larger stratiform rain amount and percentage
419 (Table 3).

420 Figures 6 and 7 show the vertical distribution of cloud species in the convective
421 and stratiform regions. The main differences between the three Goddard schemes in the
422 convective region are as follows: the Graupel scheme has more than twice as much cloud
423 ice in the upper troposphere than the Hail scheme and more than twice as much graupel
424 than the 4ICE scheme; the Hail scheme has more hail in the upper troposphere than the

425 4ICE scheme; and hail in the Hail and 4ICE schemes melts lower in the troposphere
426 (penetrating to roughly 2 km) than does graupel in the Graupel scheme (penetrating to
427 roughly 3 km). The Hail scheme has more hail below 4 km than the 4ICE, which is
428 associated with high radar reflectivities as shown below. In the stratiform region, the
429 Graupel scheme has more rain and consequently more rainfall (Table 3) than the Hail and
430 4ICE schemes. The Graupel scheme has much more graupel than 4ICE, which leads to
431 more melting and therefore more rain as well as higher conditional rain rates in the
432 stratiform region due to the higher proportion of faster falling graupel. However, snow is
433 still the most abundant ice category in all three schemes, with the Hail scheme having the
434 least amount and the 4ICE the most. The flux of snow particles through the melting layer
435 may be comparable to that of graupel in the Graupel scheme due to its slower fall speed.

436

437 3.3 *Radar reflectivity*

438 As mentioned in section 3.1, gridded radar datasets were obtained from the NMQ
439 system. Figure 8 shows time-height cross sections of the maximum reflectivity both
440 observed by radar and simulated within the model domain for each of the three NU-WRF
441 simulations from 06 to 12 UTC 20 May 2011. Simulated radar reflectivities are
442 calculated from model rain, snow, graupel and hail contents assuming inverse
443 exponential size distributions and accounting for all size and density mappings using the
444 formulation of Smith et al. [1975] and Smith [1984]. Over this period within the analysis
445 domain (Figure2), peak reflectivities associated with this intense squall line frequently
446 exceeded 50 dBZ up to 10 km and 60 dBZ below about 7 km with 40 dBZ echoes

447 reaching as high as 15 km. The maximum reflectivities do show some fluctuation but
448 overall the peak intensities are fairly steady (Figure 8a).

449 The model simulated maximum radar reflectivity is closely related to the largest
450 precipitating particles in the convective region (Figure 6). The Graupel scheme (Figure
451 8b) significantly underestimates the peak 50 to 60 dBZ intensities of the observed squall
452 line above the height of the freezing level due to the smaller size and lower density of
453 graupel. The Hail scheme produces the highest reflectivities (Figure 8c) with peak values
454 around 70 dBZ near 3-4 km and 55 dBZ values regularly reaching up to 12 km, which are
455 somewhat more intense near the melting level and above 10 km than was observed for
456 this case. These extreme dBZ values are mainly due to larger-sized hail as a result of the
457 prescribed fixed low intercept value (i.e., 0.01 cm^{-4}) for hail. The Hail scheme also
458 produces an unrealistic elevated minimum near 10 km. In contrast, the 4ICE simulation
459 (Figure 8d) produces peak reflectivity values that decrease monotonically with height in
460 best agreement with the observations, though the maximum intensities are somewhat
461 underestimated below 8 km especially earlier in the period.

462 In addition to comparing the peak reflectivities, statistical comparisons in the
463 form of contoured frequency with altitude diagrams (CFADs, see Yuter and Houze,
464 [1995]) are performed to evaluate the overall performance of each simulation with
465 respect to reflectivity. This technique computes the probability of a field as a function of
466 height. To achieve the most meaningful comparisons, the CFADs must be computed as
467 similarly as possible between the model and radar-derived fields. Comparisons between
468 the model and observations are based on a 10 min temporal resolution for each.

469 Reflectivity CFADs were constructed by binning the reflectivities into 1-dBZ bins from 0
470 to 70 dBZ at each level.

471 Figure 9a shows the observed CFAD. The highest probabilities follow a coherent
472 pattern with the peak density steadily decreasing with height from between 20 and 35
473 dBZ near the melting level to between 5 and 15 dBZ above 12 km, indicative of a robust
474 sedimentation/aggregation effect. Maximum reflectivities at the lowest frequency
475 contour of 0.001 % are just over 60 dBZ from the surface up to 6 km and drop off
476 steadily aloft to around 45 dBZ at 14 km. The Graupel scheme simulated CFAD (Figure
477 9b) has some notable discrepancies with the observed (Figure 9a). First, the Graupel
478 scheme lacks all of the reflectivity values higher than 45 dBZ above the freezing level.
479 Second, although it captures some of the aggregation effect evident in the observed
480 CFADs, it is too weak with too few echoes in the 20-25 dBZ range between 4 and 8 km.

481 The Hail scheme simulates high reflectivity values above the freezing level that
482 are closer to the observed than the Graupel scheme. It produces peak reflectivity values
483 at the lowest contour of ~65 dBZ near 4 km (melting level) that are about 5-8 dBZ higher
484 than the other two schemes (Figure 9c). Observed peak reflectivities at this frequency are
485 slightly over 61 dBZ. The Hail scheme also has an aggregation signature that deviates
486 from the observed with the area of highest probabilities shifted too high (~30 to 35 dBZ)
487 at midlevels and too low (< 10 dBZ) aloft. The 4ICE simulation, on the other hand,
488 produces a more realistic radar reflectivity CFAD with a robust and coherent aggregation
489 signature that much more closely resembles the observed. The 4ICE peak reflectivities
490 are closer to the observed and monotonically decrease with height also as observed

491 (Figure 9a and d). Below the melting level, the 4ICE scheme maintains higher peak
492 reflectivities due to melting hail in agreement with the observations.

493 Figure 10 shows the normalized degree of overlap between the observed and
494 simulated PDFs at each level where unity represents perfect overlap and zero indicates no
495 overlap between the observed and simulated reflectivity PDFs at a given level. The
496 simulated 4ICE PDFs are consistently better than the Graupel between the surface and 12
497 km and vastly better than the Hail between 5 and 14 km. The Graupel scheme is superior
498 to the Hail above the melting level but the reverse is true below. The Hail scheme has the
499 lowest scores at mid-levels due to the shift in probabilities towards 30 to 35 dBZ values
500 and the lowest scores aloft due to the shift towards weak values and having too broad of a
501 distribution. Overall, the Hail scheme has the poorest overall performance in terms of
502 CFADs, while the 4ICE clearly performs the best. Also, the 4ICE scores in NU-WRF are
503 better than those using the GCE model for this case (see Figure 7 in *Lang et al.* 2014);
504 this is likely due to the smaller domain and cyclic lateral boundaries used in the GCE
505 model, which can inhibit the size and continuity of the stratiform region.

506 There is very high occurrence of low radar reflectivity values (5-25 dBZ) in the
507 middle and upper troposphere (shown in red in Figures. 9a and d) and a low occurrence
508 of high radar reflectivities (40-60 dBZ) above 3-4 km (shown in blue in Figures. 9a and
509 d). Figure 11 shows the individual contribution of precipitating particles (rain, snow,
510 graupel and hail) to the CFAD for the 4ICE simulation. Snow is largely responsible for
511 the high occurrence of low dBZ values (Figure 11b, also see Figure 5c) and hail for the
512 low occurrence of high dBZ values aloft (Figure 11d).

513

514 3.4 *Cloud structure and vertical velocity*

515 The observations show a classic continental uni-cellular squall line structure
516 [Rutledge *et al.*, 1998; Johnson and Hamilton, 1988; see review by Houze, 1997] with
517 deep, erect leading convective cell(s) followed by a wide trailing stratiform region
518 (typical cross-section shown in Figure 12), which features a distinct high radar
519 reflectivity bright band near the melting level separated from the convective core(s) by a
520 transition area with a less prominent bright band.

521 The three NU-WRF model simulations also show a deep convective cell at the
522 leading edge followed by a wide stratiform region (typical cross-sections shown in
523 Figures 13, 14 and 15). However, there are several notable differences between the three
524 schemes as well as various discrepancies with the observations. The Graupel scheme
525 (Figure 13) produces a wider, more robust stratiform rain area than the Hail scheme
526 (Figure 14), in better agreement with the observations, but its leading edge convection is
527 much weaker than the other schemes as well as the observed. Compared to the Graupel
528 scheme, the Hail scheme (Figure 14) produces stronger leading convective cells that are
529 much more intense with high radar reflectivities above, at, and below the freezing level,
530 in better agreement with the observations, though the leading edge cells appear to be too
531 wide. However, the Hail scheme has a narrow and rather disjoint stratiform region
532 wherein the highest reflectivities are elevated in the upper troposphere rather than near or
533 below the melting layer as observed and simulated by the other schemes. These results
534 are consistent with previous GCE modeling results for a tropical convective system
535 [McCumber *et al.* [1991].

536 There are some notable improvements in the 4ICE-simulated structures (Figure
537 15) relative to the 3ICE schemes. First, in terms of the leading edge convection, the
538 simulated convective core(s) in the 4ICE scheme is more erect as observed due to the
539 inclusion of the rain evaporation correction [Li *et al.* 2009]. Also, it is both narrow and
540 intense similar to observed due to the inclusion of hail in conjunction with the elimination
541 of dry collection, whereas core intensities are too weak using the Graupel scheme and too
542 wide using the Hail scheme. Second, in terms of the trailing stratiform region, the 4ICE
543 scheme produces a broad, well developed stratiform rain area with radar reflectivity
544 values that closely match the observed and a pattern that is predominantly horizontally
545 stratified with higher values near and below the melting level. These features are in
546 much better agreement with the observations than the 3ICE schemes. The stratiform
547 region in the Graupel simulation is less horizontally stratified with more erect reflectivity
548 structures, while it is weaker and poorly organized as well as unrealistic with radar
549 echoes maximized in the upper troposphere in the Hail simulation. Finally, with the
550 inclusion of the snow breakup effect, snow sizes are kept small adjacent to the convective
551 core allowing the 4ICE scheme to capture some semblance of a transition region. The
552 observed stratiform region still covers a much larger area (~200 km) than do the
553 simulations (~75-125 km) though the Graupel and 4ICE schemes are superior to the Hail
554 scheme in this regard. All three schemes show that the convective updrafts are located at
555 the leading edge of the system above a pool of cold virtual potential temperature (Figs.
556 13-15, bottom panels). Overall, the 4ICE scheme captures more of the observed features
557 and has the most realistic structures among the three schemes.

558 Figure 16 shows CFADs of in-cloud vertical air velocity over the total, convective
559 and stratiform regions, somewhat similar to those shown in *Tao et al.* [1987, their figure
560 10]. The general features are similar for all three simulations, with upward velocities
561 exceeding 40 m/s in the mid-to-upper troposphere in the convective regions, peak
562 convective updrafts about twice as strong as the downdrafts, and higher probabilities of
563 moderate (~10 to 20 m/s) updrafts in the convective regions than in the stratiform. One
564 notable difference between the three Goddard microphysics schemes is in the stratiform
565 region where the PDFs for the Graupel scheme are appreciably wider than in the Hail and
566 4ICE schemes, meaning some of the more intense updrafts/downdrafts are being
567 classified as stratiform. Another difference is in the convective region where the Graupel
568 scheme has a higher percentage of weak-to-moderate updrafts (~5-10 m/s) in the lower
569 troposphere but a reduced proportion aloft compared to other two schemes. The
570 combination of more moderate reflectivity values and a more sheared updraft structure
571 due to the lack of a rain evaporation correction makes it more difficult to cleanly separate
572 the convective and stratiform regions in the Graupel simulation (Figure 3). This causes
573 the low level updrafts to be included in the convective region but the upper portion of
574 some of those updrafts, which are more tilted without the rain evaporation correction [cf.
575 Li et al., 2009], to be assigned to the stratiform region. Overall, the fact that the total
576 distributions are quite similar for all three schemes suggests that the larger scale shear
577 and instability features dominate microphysics scheme differences in determining the
578 updraft intensities and distribution, especially for such an unstable and sheared
579 environment.
580

581 3.5 *Comparison with previous results for the 20 May 2011 case*

582 The 20 May 2011 MC3E case was one of the cases used to help develop and
583 evaluate the new 4ICE scheme in *Lang et al.* [2014] using the GCE model. As was noted
584 previously, those GCE model simulations were forced with observed large-scale
585 advective tendencies for temperature and water vapor requiring the use of cyclic lateral
586 boundary conditions, which can complicate and inhibit the simulated spatial structures of
587 the squall line, namely the stratiform region, by allowing the leading edge convection to
588 wrap around behind the MCS (see for example Figure 2 in *Lang et al.* [2014]).
589 Restricting the stratiform area can affect the distribution of radar echoes and hence the
590 agreement between the observed and simulated radar distributions. Accordingly, CFAD
591 scores for the 4ICE scheme for this case in the GCE model study are consistently lower
592 (i.e., less than 0.75; see Figure 7 in *Lang et al.* [2014]) than they are using NU-WRF in
593 this study using the same original version of the 4ICE scheme (i.e., consistently above
594 0.8, Figure A4 or see Appendix). The ability to use a larger domain with open lateral
595 boundaries and non-uniform horizontal forcing in NU-WRF is less restrictive and
596 produces superior results and a more realistic evaluation of the 4ICE scheme.

597 *Tao et al.* [2013] examined the performance of NU-WRF for the real-time
598 forecasts during MC3E. A post mission case study was also conducted for this May 20
599 case. The results suggest that propagating precipitation features and their associated
600 cold-pool dynamics were an important physical process for the diurnal variation of
601 precipitation. Model results also indicate that terrain effects are important during the
602 initial stages of MCS development. On the other hand, surface fluxes and radiation
603 processes only have a secondary effect for short-term simulations. There are differences

604 between *Tao et al.* [2013] and the current study in terms of model configuration (18, 6
605 and 2 km vs. 9, 3 and 1 km grid spacing) and initial conditions (North American Regional
606 Reanalysis or NARR vs. Final Analysis by GFS or FNL). There are many similar results
607 between the Graupel simulation in this study and *Tao et al.* [2013]. For example, the
608 total rainfall is underestimated (see Table 5 in *Tao et al.* [2013]) as are the peak dBZ
609 values above the melting level (see Figure 10 in *Tao et al.* [2013]), in part because the
610 3ICE scheme with graupel was also used in *Tao et al.* [2013]. The vertical structure is
611 better in this study due at least in part to the higher horizontal resolution (see Figure 12 in
612 *Tao et al.*, [2013]).

613

614 **4. Summary**

615 In this study, NU-WRF was used at a relatively high horizontal resolution (i.e., 1-
616 km grid spacing for the innermost domain) to examine the performance of an improved
617 version of the new Goddard 4ICE microphysics scheme in relation to two previous 3ICE
618 versions of the Goddard microphysics (with hail and with graupel). An intense MCS that
619 was observed during MC3E was selected for this study to examine the impact of the three
620 Goddard microphysics schemes on the simulated precipitation processes associated with
621 this intense convective event and to assess simulation performance based on observed
622 radar and surface rainfall data. From a comparison of the three simulations with
623 observations, the major highlights are as follows:

- 624 • All three microphysical schemes produced a fast-propagating system (though
625 slightly too fast) with heavier rainfall at the leading edge of the convective system
626 as was observed. However, the Graupel scheme produced less heavy rainfall at

627 the leading edge of system and more light to moderate rainfall in the trailing
628 stratiform region than the 4ICE and Hail schemes and observed. The Hail scheme
629 produced less light rainfall than the other two schemes and observed. All three
630 simulations underestimated the total rainfall amount and area coverage.

631 • In terms of the rainfall pattern, the 4ICE simulation agreed better with the
632 observations than the other two simulations, with a convective leading edge more
633 intense than in the Graupel simulation and longer and more coherent than in the
634 Hail simulation. The trailing stratiform region also better ,matched observations,
635 being more coherent than in the Hail simulation and more uniform and less
636 intense than in the Graupel simulation.

637 • Both the 4ICE and Hail schemes produced more heavy precipitation (i.e., > 30-40
638 mm/h) and less moderate precipitation (i.e., 10-20 mm/h) than the Graupel
639 scheme, in better agreement with observations.

640 • The 4ICE scheme captured both the rare occurrence of high radar reflectivity
641 values (~60 dBZ) above the freezing level and the common occurrence of low
642 radar reflectivity values (5-25 dBZ) in the middle and upper troposphere,
643 including a robust sedimentation/aggregation mode (Fig. 9) seen in the
644 observations. In contrast, the Graupel scheme failed to produce reflectivity values
645 higher than 45 dBZ above the freezing level, with too few echoes in the 20-25
646 dBZ range between 4 and 8 km. The Hail scheme did produce the infrequent but
647 high reflectivity values above the freezing level in fairly good agreement with the
648 observations, but produced a disjointed and weak reflectivity mode that was
649 unlike the robust aggregation mode in the observations.

- 650 • In the 4ICE scheme results snow is mainly responsible for the high occurrence of
651 low dBZ values in the middle and upper troposphere and hail the main contributor
652 for the low occurrence of very high dBZ values aloft.
- 653 • The 4ICE scheme produced erect, narrow and intense convective cores as
654 observed, whereas intensities were too weak in the Graupel cores and too wide in
655 the Hail cores.
- 656 • The 4ICE scheme also produced a broad, well-developed, more horizontally
657 stratified stratiform rain area with radar reflectivity values that most closely
658 matched those observed. The stratiform region in the Graupel simulation was less
659 horizontally stratified with more erect reflectivity structures, while in the Hail
660 simulation it was weaker and poorly organized with unrealistic with radar echoes
661 maximized in the upper troposphere.
- 662 • All three simulations contained strong convective updrafts located at the leading
663 edge of the system, and all three schemes produced similar PDFs of vertical
664 velocity, suggesting that the larger scale shear and instability are more important
665 than changes in the microphysics scheme for determining the updraft intensities
666 and distribution in this unstable and sheared environment.

667

668 The results indicated that overall the 4ICE simulation agreed better with the
669 observations in terms of rainfall intensity, radar reflectivity, and vertical and horizontal
670 structures than did the 3ICE simulations with graupel or hail. The results also confirmed
671 the importance of hail processes for this intense summertime convective system. Hail
672 can reproduce the intense echoes above 50 dBZ; without hail, too much moderate-falling

673 graupel is transported rearward in the Graupel simulation and does not fall out in the
674 convective leading edge, whereas with the Hail scheme, “dry collection” causes some of
675 the slow-falling snow to be collected and fall out as hail in the convective leading edge.
676 The 4ICE scheme eliminates these biases by allowing only ice that was formed in a
677 manner that would produce a high-density hydrometeor (e.g., freezing drops or extreme
678 riming) to fall out as hail in the convective leading edge and therefore more slow-falling
679 snow to be transported rearward to produce a broader more uniform light rain area. In
680 addition, the evaporation correction (based on bin microphysics) helps keep the storm
681 more upright. These results are consistent with those from the GCE model [*Lang et al.*,
682 2014]. In Part II, the Goddard 4ICE scheme will be compared with other WRF
683 microphysics schemes (i.e., Morrison, WSM6, and WDM6). In addition, the Goddard
684 4ICE scheme will be implemented into the NCAR WRF for community use.

685 Simultaneously, the new 4ICE scheme has been implemented and tested in the
686 Goddard Multi-scale Modeling System (MMF), which utilizes the GCE model as the
687 cloud-precipitation parameterization within the Goddard Earth Observing System
688 (GEOS) global model. The statistical distributions of convective precipitation type has
689 been evaluated from the Goddard MMF by contrasting land and ocean regions in the
690 Tropics in comparison with TRMM signal statistics (not shown). The Goddard MMF
691 with the 4ICE scheme was able to realistically reproduce the more vigorous convective
692 characteristics over land and the shallower, weaker characteristics over ocean. MMF-
693 simulated microwave brightness temperatures show greater scattering signals over land
694 than ocean similar to the TRMM Microwave Imager (TMI), suggesting more heavily
695 rimed particles over land than ocean. This demonstrates the 4ICE scheme’s ability to

696 reproduce global statistics of land-ocean contrast in convective precipitation signals in
697 comparison with global observations. The study of different microphysical schemes from
698 the MMF shows that the new 4ICE scheme is superior to the Goddard 3ICE schemes in
699 producing realistic amounts and distributions of solid cloud and precipitating
700 hydrometeors when compared with three CloudSat/CALIPSO retrieval products (not
701 shown).
702

703 **Acknowledgments**

704 This research was supported by the NASA Precipitation Measurement Missions
705 (PMM), the NASA Modeling, Analysis, and Prediction (MAP) Program, and the Office
706 of Science (BER), U.S. Department of Energy/Atmospheric System Research
707 (DOE/ASR) Interagency Agreement (No. DE-AI02-04ER63755). NMQ (including Q2)
708 products are provided by Dr. Xiquan Dong at University of North Dakota and Carrie
709 Langston at the National Severe Storm Laboratory. The authors are grateful to Drs.
710 Ramesh Kakar and David B. Considine at NASA headquarters for their support of this
711 research. Acknowledgment is also made to the NASA Goddard Space Flight Center and
712 NASA Ames Research Center computing facilities and to Dr. Tsengdar Lee at NASA HQ
713 for the computational resources used in this research.

714

715 **References**

- 716 Brandes, E. A., K. Ikeda, G. Zhang, M. Schönhuber, and R. M. Rasmussen (2007), A
717 Statistical and Physical Description of Hydrometeor Distributions in Colorado
718 Snowstorms Using a Video Disdrometer, *J. Appl. Meteor. Climatol.*, 46, 634–650,
719 doi: <http://dx.doi.org/10.1175/JAM2489.1>.
- 720 Bryan, G. H., and H. Morrison (2012), Sensitivity of a simulated squall line to horizontal
721 resolution and parameterization of microphysics, *Mon. Wea. Rev.*, 140, 202–225.
- 722 Chin, M., R. B. Rood, S.-J. Lin, J. F. Muller, and A. M. Thomson (2000), Atmospheric
723 sulfur cycle in the global model GOCART: Model description and global properties,
724 *J. Geophys. Res.*, 105, 24,671-24,687.
- 725 Chin, M., P. Ginoux, S. Kinne, B. N. Holben, B. N. Duncan, R. V. Martin, J. A. Logan,
726 A. Higurashi, and T. Nakajima (2002), Tropospheric aerosol optical thickness from
727 the GOCART model and comparisons with satellite and sunphotometer
728 measurements, *J. Atmos. Sci.*, 59, 461-483.
- 729 Chin M., D. A. Chu, R. Levy, L. Remer, Y. Kaufman, B. Holben, T. Eck, P. Ginoux, and
730 Q. Gao (2004), Aerosol distribution in the Northern Hemisphere during ACE-Asia:
731 Results from global model, satellite observations, and Sun photometer measurements,
732 *J. Geophys. Res.*, 109, D23S90, doi:10.1029/2004GL02014.
- 733 Chou, M.-D., and M. J. Suarez (1999), A shortwave radiation parameterization for
734 atmospheric studies, 15, *NASA/TM-104606*, pp 40.
- 735 Chou, M.-D., K.-T. Lee, S.-C. Tsay, and Q. Fu (1999), Parameterization for cloud
736 longwave scattering for use in atmospheric models, *J. Climate*, 12, 159-169.

737 Colle, B. A., and Y. Zeng (2004), Bulk microphysical sensitivities within the MM5 for
738 orographic precipitation. Part I: The Sierra 1986 event, *Mon. Wea. Rev.*, 132, 2780–
739 2801.

740 Colle, B. A., M. F. Garvert, J. B. Wolfe, C. F. Mass, and C. P. Woods (2005), The 13-14
741 December 2001 IMPROVE-2 event. Part III: Simulated microphysical budgets and
742 sensitivity studies, *J. Atmos. Sci.*, 62, 3535-3558.

743 Cooper, W. A. (1986), Ice initiation in natural clouds. Precipitation Enhancement—A
744 Scientific Challenge, Meteor. Monogr. No. 43, *Amer. Meteor. Soc.*, 29–32.

745 Cotton, W. R., M. A. Stephens, T. Nehrkorn, and G. J. Tripoli (1982), The Colorado State
746 University three-dimensional cloud-mesoscale model-1982. Part II: An ice-phase
747 parameterization, *J. Rech. Atmos.*, 16, 295-320.

748 Cotton, W. R., G. J. Tripoli, R. M. Rauber, and E. A. Mulvihill (1986), Numerical
749 simulation of the effect of varying ice crystal nucleation rates and aggregation
750 processes on orographic snowfall, *J. Appl. Meteor.*, 25, 1658-1679.

751 Del Genio, A. D., J. Wu, and Y. Chen (2012), Characteristics of Mesoscale Organization
752 in WRF Simulations of Convection during TWP-ICE, *J. Climate*, 25(17), 5666-5688.

753 Dudhia, J., S.-Y. Hong, and K.-S. Lim (2008), A new method for representing mixed-
754 phase particle fall speeds in bulk microphysics parameterizations. Special Issue on
755 high-resolution cloud models, *J. Meteor. Soc. Japan*, 86A, 33-33.

756 Feng, Z., X. Dong, B. Xi, C. Schumacher, P. Minnis, and M. Khaiyer (2011), Top-of-
757 atmosphere radiation budget of convective core/stratiform rain and anvil clouds from
758 deep convective systems, *J. Geophys. Res.*, 116, D23202, doi:10.1029/2011JD016451.

759 Ferrier, B. S. (1994), A double-moment multiple-phase four-class bulk ice scheme. Part I:
760 Description, *J. Atmos. Sci.*, 51, 249-280.

761 Ferrier, B.S., W.-K. Tao and J. Simpson (1995), A double-moment multiple-phase four-
762 class bulk ice scheme. Part II: Simulations of convective storms in different large-scale
763 environments and comparisons with other bulk parameterizations, *J. Atmos Sci.*, 52,
764 1001-1033.

765 Fletcher, N. H. (1962), *The Physics of Rain Clouds. Cambridge University Press*, 386
766 pp.

767 Fovell, R. G., and Y. Ogura (1988), Numerical simulation of a midlatitude squall line in
768 two-dimensions, *J. Atmos. Sci.*, 45, 3846-3879.

769 Fridlind AM, Ackerman AS, Chaboureau J-P, Fan J, Grabowski WW, Hill AA, Jones
770 TR, Khaiyer MM, Liu G, Minnis P, Morrison H, Nguyen L, Park S, Petch JC, Pinty J-
771 P, Schumacher C, Shipway BJ, Varble AC, Wu X, Xie S, Zhang M. (2012), A
772 comparison of TWP-ICE observational data with cloud-resolving model results, *J.*
773 *Geophys. Res.* 117 :D05204, DOI: 10.1029/2011JD016595.

774 Garrett, T. J., and Coauthors (2005), Evolution of a Florida cirrus anvil, *J. Atmos. Sci.*, 62, 2352–
775 2372.

776 Gilmore, M. S., J. M. Straka, and E. N. Rasmussen (2004a), Precipitation evolution
777 sensitivity in simulated deep convective storms: Comparisons between liquid-only
778 and simple ice and liquid phase microphysics, *Mon. Wea. Rev.*, 132, 1897–1916.

779 Gilmore, M. S., J. M. Straka, and E. N. Rasmussen (2004b), Precipitation and evolution
780 sensitivity in simulated deep convective storms: comparisons between liquid-only and
781 simple ice and liquid phase microphysics, *Mon. Wea. Rev.*, 132, 1897–1916.

782 Grell, G. A., and D. Devenyi (2002), A generalized approach to parameterizing convection

783 combining ensemble and data assimilation techniques, *Geophys. Res. Lett.*, 29, Article
784 1693.

785 Griggs, D. J., and T. W. Choullarton (1986), A laboratory study of secondary ice particle
786 production by the fragmentation of rime and vapour-grown ice crystals, *Q. J. R.*
787 *Meteor. Soc.*, 112, 149-163.

788 Guy, N., X. Zeng, S. A. Rutledge, W.-K. Tao (2013), Comparing the convective structure
789 and microphysics in two Sahelian mesoscale convective systems: Radar observations
790 and CRM simulations, *Mon. Wea. Rev.*, 141, 582–601.

791 Han, M., S. A. Braun, T. Matsui, and C. R. Williams (2013), Evaluation of cloud
792 microphysics schemes in simulations of a winter storm using radar and radiometer
793 measurements, *J. Geophys. Res. Atmos.*, 118, 1401–1419, doi: [10.1002/jgrd.50115](https://doi.org/10.1002/jgrd.50115).

794 Hallet, J. and S. C. Mossop (1974), Production of secondary ice particles during the
795 riming process, *Nature*, 249, 26–28.

796 Hobbs, P. V. (1969), Ice Multiplication in Clouds. *J. Atmos. Sci.*, 26, 315–318,
797 doi: [http://dx.doi.org/10.1175/1520-0469\(1969\)026<0315:IMIC>2.0.CO;2](http://dx.doi.org/10.1175/1520-0469(1969)026<0315:IMIC>2.0.CO;2).

798 Hobbs, P. V. (1974), High concentrations of ice particles in a layer cloud, *Nature*, 251,
799 694–696.

800 Hobbs, P. V., and A. L. Rangno (1985), Ice Particle Concentrations in Clouds, *J. Atmos.*
801 *Sci.*, 42, 2523–2549. doi: [http://dx.doi.org/10.1175/1520-](http://dx.doi.org/10.1175/1520-0469(1985)042<2523:IPCIC>2.0.CO;2)
802 [0469\(1985\)042<2523:IPCIC>2.0.CO;2](http://dx.doi.org/10.1175/1520-0469(1985)042<2523:IPCIC>2.0.CO;2).

803 Hong, S.-Y., J. Dudhia, and S.-H. Chen (2004), A revised approach to ice microphysical
804 processes for the bulk parameterization of clouds and precipitation, *Mon. Wea. Rev.*,
805 132, 103-120.

806 Hong, S.-Y., and J.-O. J. Lim (2006), The WRF Single-Moment 6-Class Microphysics
807 Scheme (WSM6), *J. Korean Meteor. Soc.*, 42, 2, 129-151.

808 Hong, S.-Y., K.-S. Lim, J.-H. Kim, J.-O. Lim, and J. Dudhia (2009), Sensitivity study of
809 the cloud-resolving convective simulations with WRF using two-bulk microphysical
810 parameterizations: Ice-phase microphysics versus sedimentation effects, *J. Appl.*
811 *Meteor. Clim.*, 48, 61-76.

812 Houze, R. A., Jr. (1997), Stratiform precipitation in regions of convection: A
813 meteorological paradox?, *Bull. Amer. Meteor. Soc.*, 78, 2179-2196.

814 Iguchi, T., T. Matsui, J. J. Shi, W.-K. Tao, A. P. Khain, A. Hou, R. Cifelli, A.
815 Heymsfield, and A. Tokay (2012a), Numerical analysis using WRF-SBM for the
816 cloud microphysical structures in the C3VP field campaign: Impacts of supercooled
817 droplets and resultant riming on snow microphysics, *J. Geophys. Res.*, 117, D23206,
818 doi:[10.1029/2012JD018101](https://doi.org/10.1029/2012JD018101).

819 Iguchi, T., T. Matsui, A. Tokay, P. Kollias, and W.-K. Tao (2012b), Two distinct modes
820 in one-day rainfall event during MC3E field campaign: Analyses of disdrometer
821 observations and WRF-SBM simulation, *Geophys. Res. Lett.*, 39, L24805,
822 doi:[10.1029/2012GL053329](https://doi.org/10.1029/2012GL053329).

823 Iguchi, T., T. Matsui, W.-K. Tao, A. Khain, V. T. J. Phillips, C. Kidd, T. L'Ecuyer, S. A.
824 Braun, A. Hou, and M. R. Schwaller (2014), Numerical simulations using WRF-SBM
825 for mixed-phase precipitation and consequent bright band structure observed in the
826 LPVEx field campaign, *J. Applied Meteor. Climatol.*, 53, 2710-2731,
827 doi:[10.1175/JAMC-D-13-0334.1](https://doi.org/10.1175/JAMC-D-13-0334.1).

828 Jankov, I., W. A. Gallus Jr., M. Segal, B. Shaw, S. E. Koch (2005), The impact of
829 different WRF model physical parameterizations and their interactions on warm
830 season MCS rainfall, *Wea. Forecasting*, 6, 1048-1060.

831 Jankov, I., W. A. Gallus Jr., M. Segal, B. Shaw, S. E. Koch (2007), Influence of initial
832 conditions on the WRF-ARW model QPF response to physical parameterization
833 changes, *Wea. Forecasting*, 22, 501-519.

834 Jensen, E., O. Toon, S. Vay, J. Ovarlez, R. May, T. Bui, C. Twohy, B. Gandrud, R.
835 Pueschel, and U. Schumann (2001), Prevalence of ice-supersaturated regions in the
836 upper troposphere: Implications for optically thin ice cloud formation, *J. Geophys.*
837 *Res.*, 106(D15), 17253-17266.

838 Johnson, R. H., and P. J. Hamilton (1988), The relationship of surface pressure features
839 to the precipitation and air flow structure of an intense midlatitude squall line, *Mon.*
840 *Wea. Rev.*, 116, 1444-1472.

841 Khairoutdinov, M., and D. Randall (2006), High-resolution simulation of shallow-to-deep
842 convection transition over land, *J. Atmos. Sci.*, 63, 3421-3436.

843 Krueger, S. K., Q. A. Fu, K. N. Liou, and H. N. S. Chin (1995), Improvements of an ice-
844 phase microphysics parameterization for use in numerical simulations of tropical
845 convection, *J. Appl. Meteor.*, 34, 281-287.

846 Kumar, S. V., C. D. Peters-Lidard, Y. Tian, J. Geiger, P. R. Houser, S. Olden, L. Lighty,
847 J. L. Eastman, P. Dirmeyer, B. Doty, J. Adams, E. Wood, and J. Sheffield (2006), LIS
848 - An Interoperable Framework for High Resolution Land Surface Modeling,
849 *Environmental Modeling & Software*, 21, 1402-1415.

850 Lang, S., W.-K. Tao, J. Simpson, and B. Ferrier (2003), Modeling of convective-
851 stratiform precipitation processes: Sensitivity to partitioning methods, *J. Appl.*
852 *Meteor.*, 42, 505-527.

853 Lang, S., W.-K. Tao, R. Cifelli, W. Olson, J. Halverson, S. Rutledge, and J. Simpson
854 (2007), Improving simulations of convective system from TRMM LBA: Easterly and
855 Westerly regimes, *J. Atmos. Sci.*, 64, 1141-1164.

856 Lang, S. E., W.-K. Tao, X. Zeng, and Y. Li (2011), Reducing the biases in simulated
857 radar reflectivities from a bulk microphysics scheme: Tropical convective systems,
858 *J. Atmos. Sci.*, 68, 2306–2320.

859 Lang, S., W.-K. Tao, J.-D. Chern, D. Wu, and X. Li (2014), Benefits of a 4th ice class in
860 the simulated radar reflectivities of convective systems using a bulk microphysics
861 scheme, *J. Atmos. Sci.*, 71, 3583-3612.

862 Levin, Z. and W.R. Cotton (Eds.) (2008), Aerosol Pollution Impact on Precipitation; A
863 scientific review, *Springer Press.*, 382 pp.

864 Li, X., and Z. Pu (2008), Sensitivity of numerical simulation of early rapid intensification
865 of hurricane Emily (2005) to cloud microphysical and planetary boundary layer
866 parameterization, *Mon. Wea. Rev.*, 136, 4819-4838.

867 Li, X., W.-K. Tao, A. P. Khain, J. Simpson, D. E. Johnson (2009), Sensitivity of a cloud-
868 resolving model to bulk and explicit bin microphysical schemes. Part II: Cloud
869 microphysics and storm dynamics interactions, *J. Atmos. Sci.*, 66, 22–40.

870 Li, X., W.-K. Tao, T. Matsui, C. Liu, and H. Masunaga (2010), Improving a spectral bin
871 microphysical scheme using long-term TRMM satellite observations, *Quart. J. Roy.*
872 *Meteoro. Soc.*, 136, 382-399.

873 Li, Y., E. J. Zipser, S. K. Krueger, and M. A. Zulauf (2008), Cloud-resolving modeling of
874 deep convection during KWAJEX. Part I: Comparison to TRMM satellite and
875 ground-based radar observations, *Mon. Wea. Rev.*, 136, 2699-2712.

876 Lim, K.-S. S., and S.-Y. Hong (2010), Development of an effective double-moment cloud
877 microphysics scheme with prognostic cloud condensation nuclei (CCN) for weather
878 and climate models, *Mon. Wea. Rev.*, 138, 1587–1612.

879 Lin, Y.-L., R. D. Farley, and H. D. Orville (1983), Bulk parameterization of the snow
880 field in a cloud model, *J. Climate Appl. Meteor.*, 22, 1065-1092.

881 Lin, Y., B. A. Colle (2011), A new bulk microphysical scheme that includes riming
882 intensity and temperature-dependent ice characteristics, *Mon. Wea. Rev.*, 139, 1013–
883 1035.

884 Lin, Y.-L., R. D. Farley and H. D. Orville (1983), Bulk parameterization of the snow field
885 in a cloud model, *J. Clim. Appl. Meteor.*, 22, 1065-1092.

886 Liu, Y., D.-L. Zhang, and M. K. Yau (1997), A multiscale numerical study of Hurricane
887 Andrew (1992). Part I: An explicit simulation, *Mon. Wea. Rev.*, 125, 3073-3093.

888 Lo, K. Kenneth, and R. E. Passarelli (1982), The growth of snow in winter storms: An
889 airborne observational study, *J. Atmos. Sci.*, 39, 697–706.

890 Lord, S. J., H. E. Willoughby and J. M. Piotrowicz (1984), Role of a parameterized ice-
891 phase microphysics in an axisymmetric, non-hydrostatic tropical cyclone model, *J.*
892 *Atmos. Sci.*, 41, 2836-2848.

893 Luo, Y., Y. Wang, H. Wang, Y. Zheng, and H. Morrison (2010), Modeling Convective-
894 Stratiform Precipitation Processes on a Mei-Yu Front with the Weather Research and

895 Forecasting Model: Comparison with Observations and Sensitivity to Cloud
896 Microphysics Parameterizations, *J. Geophys. Res.*, 115, D18117.

897 Matsui, T. T. Iguchi, X. Li, M. Han, W.-K. Tao, W. Petersen, T. L'Ecuyer, R. Meneghini,
898 W. Olson, C. D. Kummerow, A. Y. Hou, M. R. Schwaller, E. F. Stocker, J.
899 Kwiatkowski (2013), GPM satellite simulator over ground validation sites, *Bull.*
900 *Amer. Meteor. Soc.*, 94, 1653–1660. doi: [http://dx.doi.org/10.1175/BAMS-D-12-](http://dx.doi.org/10.1175/BAMS-D-12-00160.1)
901 00160.1

902 McCumber, M., W.-K. Tao, J. Simpson, R. Penc, and S.-T. Soong (1991), Comparison of
903 ice-phase microphysical parameterization schemes using numerical simulations of
904 tropical convection, *J. Appl. Meteor.*, 30, 985-1004.

905 Mellor, G. L., and T. Yamada (1982), Development of a turbulence closure model for
906 geophysical fluid problems, *Rev. Geophys. Space Phys.*, 20, 851-875.

907 Meyers, M. P., P. J. DeMott, and W. R. Cotton (1992), New primary ice-nucleation
908 parameterizations in an explicit cloud model, *J. Appl. Meteor.*, 31, 708–721.

909 Meyers, M. P., R. L. Walko, J. Y. Harrington, and W. R. Cotton (1997), New RAMS
910 cloud microphysics parameterization. Part II: The two-moment scheme, *Atmos. Res.*,
911 45, 3–39.

912 Milbrandt, J. A., and M. K. Yau (2005a), A multimoment bulk microphysics
913 parameterization. Part I: Analysis of the role of the spectral shape parameter, *J.*
914 *Atmos. Sci.*, 62, 3051–3064.

915 Milbrandt, J. A., and M. K. Yau (2005b) A multimoment bulk microphysics
916 parameterization. Part II: A proposed three-moment closure and scheme description,
917 *J. Atmos. Sci.*, 62, 3065–3081.

918 Milbrandt, J. A., and H. Morrison (2013), Prediction of graupel density in a bulk
919 microphysics scheme, *J. Atmos. Sci.*, 70, 410–429.

920 Moncrieff, M. W., S. K. Krueger, D. Gregory, J.-L. Redelsperger and W.-K. Tao (1997),
921 GEWEX Cloud System Study (GCSS) Working Group 4: Precipitating convective
922 cloud systems, *Bull. Amer. Meteor. Soc.*, 78, 831-845.

923 Molthan, A. L., and B. A. Colle (2012), Comparisons of single- and double-moment
924 microphysics schemes in the simulation of a synoptic-scale snowfall event, *Mon.*
925 *Wea. Rev.*, 140, 2982–3002.

926 Morrison, H., J. A. Curry, and V. I. Khvorostyanov (2005), A new double-moment
927 microphysics parameterization for application in cloud and climate models. Part I:
928 Description, *J. Atmos. Sci.*, 62, 1665-1677.

929 Morrison, H., and W. W. Grabowski (2007), Comparison of bulk and bin warm-rain
930 microphysics models using a kinematic framework, *J. Atmos. Sci.*, 64 (8), 2839–2861.

931 Morrison, H., and W. Grabowski (2008), A Novel Approach for Representing Ice
932 Microphysics in Models: Description and Tests Using a Kinematic Framework, *J.*
933 *Atmos. Sci.*, 65, 1528-1548.

934 Morrison, H., G. Thompson, and V. Tatarskii (2009), Impact of cloud microphysics on
935 the development of trailing stratiform precipitation in a simulated squall line:
936 Comparison of one- and two-moment schemes, *Mon. Wea. Rev.*, 137, 991–1007.

937 Morrison, H., and J. A. Milbrandt (2011), Comparison of two-moment bulk microphysics
938 schemes in idealized supercell thunderstorm simulations, *Mon. Wea. Rev.*, 139, 1103–
939 1130.

940 Morrison, H., and J. A. Milbrandt (2015), Parameterization of cloud microphysics based
941 on the prediction of bulk ice particle properties. Part I: Scheme description and
942 idealized tests, *J. Atmos. Sci.*, 72, 287-311.

943 Morrison, H., J. A. Milbrandt, G. H. Bryan, K. Ikeda, S. A. Tessendorf, and G.
944 Thompson (2015), Parameterization of cloud microphysics based on the prediction of
945 bulk ice particle properties, *J. Atmos. Sci.*, 72, 312-339.

946 Mossop, S. C., R. E. Ruskin, K. J. Heffernan (1968), Glaciation of a cumulus at
947 approximately -4C , *J. Atmos. Sci.*, 25, 889–899.
948 doi: [http://dx.doi.org/10.1175/1520-0469\(1968\)025<0889:GOACAA>2.0.CO;2](http://dx.doi.org/10.1175/1520-0469(1968)025<0889:GOACAA>2.0.CO;2).

949 Mossop, S. C., Cottis, R. E. and Bartlett, B. M. (1972) Ice crystal concentrations in
950 cumulus and stratocumulus clouds, *Q. J. R. Meteor. Soc.*, 98: 105–123.
951 doi: 10.1002/qj.49709841509

952 Muhlbauer, A., and coauthors (2013), Reexamination of the state of the art of cloud
953 modeling shows real improvements, *Bull. Amer. Meteor. Soc.*, 94, ES45–ES48.

954 Nicholls, M. E. (1987), A comparison of the results of a two-dimensional numerical
955 simulation of a tropical squall line with observations, *Mon. Wea. Rev.*, 115, 3055–
956 3077.

957 Olson, W.-S., C. D. Kummerow,, S. Yang, G. W. Petty, W.-K. Tao, T. L. Bell, S. A.
958 Braun, Y. Wang, S. E. Lang, D. E. Johnson and C. Chiu (2006), Precipitation and
959 latent heating distributions from satellite passive microwave radiometry Part I: Method
960 and uncertainties, *J. Applied Meteor.*, 45, 702-720.

961 Oraltay, R. G., J. Hallet (1989), Evaporation and melting of ice crystals: A laboratory
962 study, *Atmos. Res.*, 24, 169–189.

963 Peters-Lidard, C.D., E. M. Kemp, T. Matsui, J. A. Santanello, Jr., S. V., Kumar, J. Jacob,
964 T. Clune, W.-K. Tao, M. Chin, A. Hou, J. L. Case,, D. Kim, K.-M. Kim, W. Lau, Y.
965 Liu, J.-J. Shi, D. Starr, Q. Tan,, Z. Tao, B. Zaitchik, B. Zavodsky, S. Zhang, M.
966 Zupanski (2014), Integrated Modeling of Aerosol, Cloud, Precipitation and Land
967 Processes at Satellite-Resolved Scales with the NASA Unified-Weather Research and
968 Forecasting Model, *Environmental Modeling & Software*, 67,149-159.
969 doi:<http://dx.doi.org/10.1016/j.envsoft.2015.01.007>.

970 Petersen, W. A., and M. Jensen (2012), The NASA-GPM and DOE-ARM Midlatitude
971 Continental Convective Clouds Experiment (MC3E), *Earth Observer*, 24, 12-18,
972 [http://pmm.nasa.gov/sites/default/files/document_files/Earth_Observer_Jan_2012_M](http://pmm.nasa.gov/sites/default/files/document_files/Earth_Observer_Jan_2012_MC3E.pdf)
973 [C3E.pdf](http://pmm.nasa.gov/sites/default/files/document_files/Earth_Observer_Jan_2012_MC3E.pdf).

974 Powell, S. W., R. A. Houze, Jr., A. Kumar, S. A. McFarlane (2012), Comparison of
975 simulated and observed continental tropical anvil clouds and their radiative heating
976 profiles, *J. Atmos. Sci.*, 69, 2662–2681.

977 Prasad, N., H.-Y. M. Yeh, R. F. Adler and W.-K. Tao (1995), Infrared and microwave
978 simulations of an intense convective system and comparison with aircraft
979 observations, *J. Appl. Meteor.*, 34, 153-174.

980 Reisin, T., Z. Levin, and S. Tzivion (1996), Rain production in convective clouds as
981 simulated in an axisymmetric model with detailed microphysics. Part I: Description
982 of the model, *J. Atmos. Sci.*, 53, 497–519.

983 Reisner, J. R., R. M. Rasmussen, and R. T. Bruintjes (1998), Explicit forecasting of
984 supercooled liquid water in winter storms using the MM5 mesoscale model, *Quart. J.*
985 *Roy. Meteor. Soc.*, 124, 1071-1107.

986 Rutledge, S.A., and P.V. Hobbs (1984), The mesoscale and microscale structure and
987 organization of clouds and precipitation in mid-latitude clouds. Part XII: A diagnostic
988 modeling study of precipitation development in narrow cold frontal rainbands, *J.*
989 *Atmos. Sci.*, 41, 2949-2972.

990 Rutledge, S. A., R. A. Houze, Jr., and M. I. Biggerstaff (1988), The Oklahoma-Kansas
991 mesoscale convective system of 10-11 June 1985: Precipitation structure and single-
992 doppler radar analysis, *Mon. Wea. Rev.*, 116, 1409-1430.

993 Santanello, J. A. Jr, C. D. Peters-Lidard, S. V. Kummar, C. Alonge, and W.-K. Tao
994 (2009), A modeling and observational framework for diagnosing local land-
995 atmosphere coupling on diurnal time scales, *J. of Hydrometeor*, 10, 577-599.

996 Seifert, A., and K. D. Beheng (2006), A two-moment cloud microphysics
997 parameterization for mixed-phase clouds. Part 1: Model description, *Meteor. Atmos.*
998 *Phys.*, 92, 45–66.

999 Shi, J. J., W.-K. Tao, T. Matsui, A. Hou, S. Lang, C. Peters-Lidard, G. Jackson, R.
1000 Cifelli, S. Rutledge, and W. Petersen (2010), Microphysical Properties of the January
1001 20-22 2007 Snow Events over Canada: Comparison with in-situ and Satellite
1002 Observations, *J. Applied Meteor. Climatol*, 49, 2246-2266

1003 Shi, J. J., T. Matsui, W.-K. Tao, C. Peters-Lidard, M. Chin, Q. Tan, and E. Kemp (2014),
1004 The impact of aerosol on precipitation processes associated with an NAMMA
1005 mesoscale convective system, *Quart. J. Royal Meteor. Soc.*, 140, 2158-2175.
1006 doi: 10.1002/qj.2286.

1007 Smith, P. L., Jr., C. G. Meyers, and H. D. Orville (1975), Radar reflectivity factor
1008 calculations in numerical cloud models using bulk parameterization of precipitation,
1009 *J. Appl. Meteor.*, 14, 1156-1165.

1010 Smith, P. L. (1984), Equivalent radar reflectivity factors for snow and ice particles, *J.*
1011 *Climate and Appl. Meteor.*, 23, 1258-1260.

1012 Steiner, M., R. A. Houze Jr., and S. E. Yuter (1995), Climatological characteristics of
1013 three-dimensional storm structure from operational radar and rain gauge data, *J. Appl.*
1014 *Meteor.*, 34, 1978-2007.

1015 Straka, J. M., and E. R. Mansell (2005), A bulk microphysics parameterization with
1016 multiple ice precipitation categories, *J. Appl. Meteor.*, 44, 445-466.

1017 Stith, J. L., J. E. Dye, A. Bansemer, A. J. Heymsfield, C. A. Grainger, W. A. Petersen,
1018 and R. Cifelli (2002), Microphysical observations of tropical clouds, *J. Appl. Meteor.*,
1019 41, 97-117.

1020 Takahashi, T., Y. Nagao, and Y. Kushiya (1995), Possible high ice particle production
1021 during graupel–graupel collisions, *J. Atmos. Sci.*, 52, 4523–4527.

1022 Tang, L., Y. Tian, and X. Lin (2014), Validation of precipitation retrievals over land from
1023 satellite-based passive microwave sensors, *J. Geophys. Res. Atmos.*, 119, 4546 –4567,
1024 doi:10.1002/2013JD020933.

1025 Tao, W.-K., J. Simpson, and S.-T. Soong (1987), Statistical properties of a cloud
1026 ensemble: A numerical study, *J. Atmos. Sci.*, 44, 3175-3187.

1027 Tao, W.-K., and J. Simpson (1989), Modeling study of a tropical squall-type convective
1028 line, *J. Atmos. Sci.*, 46, 177-202.

1029 Tao, W.-K., J. Simpson and M. McCumber (1989), An ice-water saturation adjustment,

1030 *Mon. Wea. Rev.*, 117, 231-235.

1031 Tao, W.-K., and J. Simpson (1993), The Goddard Cumulus Ensemble Model. Part I:
1032 Model description, *Terrestrial, Atmospheric and Oceanic Sciences*, 4, 19-54.

1033 Tao, W.-K., J. Scala, B. Ferrier and J. Simpson (1995), The effects of melting processes
1034 on the development of a tropical and a midlatitude squall line, *J. Atmos. Sci.*, 52,
1035 1934-1948.

1036 Tao, W.-K., J. Simpson, D. Baker, S. Braun, M.-D. Chou, B. Ferrier, D. Johnson, A.
1037 Khain, S. Lang, B. Lynn, C.-L. Shie, D. Starr, C.-H. Sui, Y. Wang and P. Wetzel
1038 (2003), Microphysics, radiation and surface processes in the Goddard Cumulus
1039 Ensemble (GCE) model, A Special Issue on Non-hydrostatic Mesoscale Modeling,
1040 *Meteorology and Atmospheric Physics*, 82, 97-137.

1041 Tao, W.-K., J. J. Shi, S. S. Chen, S. Lang, P.-L. Lin, S.-Y. Hong, C. Peters-Lidard and A.
1042 Hou (2011), The impact of microphysical schemes on hurricane intensity and track.
1043 Special Issue on MCSs and High-Impact Weather/Climate in East Asia, *Asia-Pacific*
1044 *J. Atmos. Sci. (APJAS)*, 47, 1-16.

1045 Tao, W.-K., J. J. Shi, P.-L. Lin, J. Chen, S. Lang, M.-Y. Chang, M.-J. Yang, C.-C. Wu,
1046 C. Peter-Lidard, C.-H. Sui, and B. J.-D. Jou (2011), High Resolution Numerical
1047 Simulation of the extreme rainfall associated with Typhoon Morakot: Part I: Impact
1048 of Microphysics and PBL, Special Issue on Typhoon Morakot, *Terrestrial,*
1049 *Atmospheric and Oceanic Sciences*, Vol. 22, No. 6, 673-696.
1050 doi.10.3319/TAO2011.08.26.01

1051 Tao, W.-K., D. Wu, T. Matsui, C. Peters-Lidard, S. Lang, A. Hou, M. Rienecker, W.
1052 Petersen, and M. Jensen (2013), Precipitation intensity and variation during MC3E:

1053 A numerical modeling study, *J. Geophys. Res. Atmos.*, 118, 7199–7218,
1054 doi:10.1002/jgrd.50410.

1055 Tao, W.-K., S. Lang, X. Zeng, X. Li, T. Matsui, K. Mohr, D. Posselt, J. Chern, C. Peters-
1056 Lidard, P. Norris, I.-S. Kang, I. Choi, A. Hou, K.-M. Lau, and Y.-M. Yang (2014),
1057 The Goddard Cumulus Ensemble model (GCE): Improvements and applications for
1058 studying precipitation processes, *An invited paper - Atmos. Res.*, 143, 392-424.

1059 Tao, W.-K., and M. Moncrieff (2009), Multi-scale cloud-system modeling, *Rev. Geophys.*,
1060 47, RG4002, doi:10.1029/2008RG000276.

1061 Thompson, G., R. M. Rasmussen, and K. Manning (2004), Explicit forecasts of winter
1062 precipitation using an improved bulk microphysics scheme. Part I: Description and
1063 sensitivity analysis, *Mon. Wea. Rev.*, 132, 519-542.

1064 Thompson, G., P. R. Field, R. M. Rasmussen, and W. D. Hall (2008), Explicit forecasts of
1065 winter precipitation using an improved bulk microphysics scheme. Part II:
1066 Implementation of a new snow parameterization, *Mon. Wea. Rev.*, 136, 5095-5155.

1067 Van Weverberg, K., and Coauthors (2013), The role of cloud microphysics
1068 parameterization in the simulation of mesoscale convective system clouds and
1069 precipitation in the tropical western pacific, *J. Atmos. Sci.*, 70, 1104–1128.

1070 Van Weverberg K, NP van Lipzig, L Delobbe, and AM Vogelmann (2012), The role of
1071 precipitation size distributions in km-scale NWP simulations of intense precipitation:
1072 evaluation of cloud properties and surface precipitation, *Quart. J. Royal Meteor. Soc.*,
1073 138, doi:10.1002/qj.1933.

1074 Van Weverberg K, AM Vogelmann, H Morrison, and JA Milbrandt (2012), Sensitivity of
1075 idealized squall-line simulations to the level of complexity used in two-moment bulk
1076 microphysics schemes, *Mon. Wea. Rev.*, 140(6), doi:10.1175/MWR-D-11-00120.1

1077 Van Weverberg K. (2013), Impact of environmental instability on convective
1078 precipitation uncertainty associated with the nature of the rimed ice species in a bulk
1079 microphysics scheme, *Mon. Wea. Rev.*, , doi:10.1175/MWR-D-13-00036.1.

1080 Vardiman, L. (1978), The generation of secondary ice particles in clouds by crystal-
1081 crystal collision, *J. Atmos. Sci.*, 35, 2168–2180.
1082 doi: [http://dx.doi.org/10.1175/1520-0469\(1978\)035<2168:TGOSIP>2.0.CO;2](http://dx.doi.org/10.1175/1520-0469(1978)035<2168:TGOSIP>2.0.CO;2)

1083 Walko, R. L., W. R. Cotton, M. P. Meyers, and J. Y. Harrington (1995), New RAMS
1084 cloud microphysics parameterization Part I: the single-moment scheme, *Atmos. Res.*,
1085 38, 29-62.

1086 Wang, Y. (2002), An explicit simulation of tropical cyclones with a triply nested movable
1087 mesh primitive equations model-TCM3. Part II: Model refinements and sensitivity to
1088 cloud microphysics parameterization, *Mon. Wea. Rev.*, 130, 3022-3036.

1089 Wu X., W. D. Hall, W. W. Grabowski, M. W. Moncrieff, W. D. Collins, and J. T. Kiehl
1090 (1999), Long-term behavior of cloud systems in TOGA COARE and their interactions
1091 with radiative and surface processes. Part II: Effects of ice microphysics on cloud-
1092 radiation interaction, *J. Atmos. Sci.*, 56, 3177–3195.

1093 Wu, D., X. Dong, B. Xi, Z. Feng, A. Kennedy, G. Mullendore, M. Gilmore, and W.-K.
1094 Tao (2013), Impacts of microphysical scheme on convective and stratiform
1095 characteristics in two high precipitation squall line events, *J. Geophys. Res. Atmos.*,
1096 118, doi:10.1002/jgrd.50798.

- 1097 Yano, J.-I., V. T. J. Phillips (2011), Ice–ice collisions: An ice multiplication process in
1098 atmospheric clouds, *J. Atmos. Sci.*, 68, 322–333.
1099 doi: <http://dx.doi.org/10.1175/2010JAS3607.1>
- 1100 Yeh, H.-Y. M., N. Prasad, R. Meneghini, W.-K. Tao and R. F. Adler (1995), Model-based
1101 simulation of TRMM spaceborne radar observations, *J. Appl. Meteor.*, 34, 175-197.
- 1102 Yoshizaki, M. (1986), Numerical simulations of tropical squall-line clusters: Two-
1103 dimensional model, *J. Meteor. Soc. Japan*, 64, 469–491.
- 1104 Yuter, S. E., and Houze R. A. Jr. (1995), Three-dimensional kinematic and microphysical
1105 evolution of Florida cumulonimbus. Part II: Frequency distributions of vertical
1106 velocity, reflectivity, and differential reflectivity, *Mon. Wea. Rev.*, 123, 1941–1963.
- 1107 Zhang, J., et al. (2011), National mosaic and multi-sensor QPE (NMQ) system:
1108 Description, results, and future plans, *Bull. Am. Meteorol. Soc.*, 92, 1321–1338.
- 1109 Zhang, P., D. Zrnica, and A. Ryzhkov (2011), Verification of Beam Blockage Correction
1110 by Comparison Between Radar QPE and Rain Gage Measurement, *NOAA/NSSL*
1111 *report*, 7 pp.
- 1112 Zhu, T., and D.-L. Zhang (2006a), Numerical simulation of Hurricane Bonnie (1998). Part
1113 II: Sensitivity to varying cloud microphysical processes, *J. Atmos. Sci.*, 63, 109-126.
- 1114 Zhu, T., and D.-L. Zhang (2006b), The impact of the storm-induced SST cooling on
1115 hurricane intensity, *Adv. Atmos. Sci.*, 23, 14-22.

1116 **Appendix: Description of the Goddard Microphysics schemes**

1117 The original Goddard two-class liquid and three-class ice microphysics scheme
1118 developed and coded at Goddard [Tao and Simpson, 1993] was mainly based on Lin *et*
1119 *al.* [1983] with additional processes from Rutledge and Hobbs [1984]. Modifications

1120 were also made to better address saturation issues [Tao *et al.*, 2003]. This scheme has
1121 undergone several progressive revisions, culminating in an updated version of the 4ICE
1122 scheme currently used in this study. Details of these improvements are as follows.

1123

1124 (A.1) *Lang et al. [2007] – 3ICE scheme*

1125 Lang *et al.* [2007] showed that eliminating dry collection by graupel in the
1126 Goddard 3ICE-graupel bulk microphysics scheme effectively reduced the unrealistic
1127 presence of graupel in the simulated anvil. However, comparisons with radar reflectivity
1128 data using CFADs revealed that the resulting snow contents were too large. The
1129 excessive snow was reduced primarily by lowering the collection efficiency of cloud
1130 water by snow and resulted in further agreement with the radar observations. The
1131 transfer of cloud-sized particles to precipitation-sized ice appeared to be too efficient in
1132 the original scheme. Overall, these changes to the microphysics lead to more realistic
1133 precipitation ice contents in the model and as a consequence more physically realistic
1134 hydrometeor profiles for radiance calculations for remote sensing applications.

1135

1136 (A.2) *Lang et al. [2011] - 3ICE scheme*

1137 The performance of the GCE bulk microphysics scheme was further improved by
1138 reducing the bias in over penetrating 40-dBZ echoes at higher altitudes due mainly to
1139 excessively large contents and/or sizes of graupel particles at those altitudes [Lang *et al.*,
1140 2011]. These improvements were achieved by systematically evaluating and improving
1141 individual ice processes, namely: (1) accounting for relative humidity and mean cloud
1142 ice mass in the Bergeron process for snow, (2) adding a simple Hallett-Mossop rime

1143 splintering parameterization, (3) replacing the Fletcher curve, which determines the
1144 number of active ice nuclei (IN) as a function of temperature, with the Meyers *et al.*
1145 [1992] curve, which determines the active IN as a function of ice supersaturation, in the
1146 cloud ice nucleation, depositional growth and Bergeron growth parameterizations, (4)
1147 relaxing the saturation scheme to allow for ice supersaturation, (5) adding two additional
1148 parameterizations for contact nucleation and immersion freezing, (6) including cloud ice
1149 fall speeds, (7) allowing graupel and snow to sublimate (the original Rutledge and Hobbs
1150 scheme only allows graupel and snow deposition but not sublimation, and (8) mapping
1151 the snow and graupel intercepts (effectively the mean snow and graupel particle
1152 diameters) as functions of temperature and mass. These changes also improved the
1153 overall model reflectivity probability distributions (i.e., CFADs).

1154

1155 *(A.3) Lang et al. [2014] – 4ICE scheme*

1156 The Goddard Rutledge and Hobbs-based 3ICE scheme (cloud ice, snow and
1157 graupel) was then enhanced by the addition of hail processes and further modified to
1158 produce a new 4ICE scheme (cloud ice, snow, graupel, and hail) capable of simulating
1159 both intense and moderate convection. Hail processes taken from the 3ICE-hail scheme
1160 based on Lin et al. [1983] included hail riming, accretion of rain, deposition/sublimation,
1161 melting, shedding and wet growth. Hail dry collection was eliminated to prevent the
1162 same excessive buildup of hail as had occurred previously with graupel [Lang et al.,
1163 2007]; however, hail near wet growth is allowed to efficiently collect other ice particles.
1164 Processes that freeze rain now initiate hail (high density ice) not graupel. Four new hail
1165 processes were added: wet hail accretion of graupel, rime splintering via hail riming, hail

1166 conversion to snow via deposition at colder temperatures (also applied to graupel), and
1167 hail conversion to graupel due to riming under non wet growth conditions. Besides the
1168 hail processes, further modifications were made to the 3ICE processes, including
1169 allowing greater ice supersaturation and mitigating spurious evaporation/sublimation in
1170 the saturation adjustment scheme and the inclusion of a bin microphysics-based [Li et al.,
1171 2009] rain evaporation correction but with physical raindrop size constraints and a vapor
1172 diffusivity factor. The improved 3ICE snow/graupel size-mapping schemes were
1173 adjusted to be more stable at higher mixing ratios and to increase the aggregation effect
1174 for snow. A snow density mapping [Brandes et al., 2007] was also added. The resulting
1175 4ICE scheme was shown to perform well not only for the intense MC3E 20 May squall
1176 line case presented in this study but also for less organized moderate convection observed
1177 during TRMM LBA. Not only were the 4ICE radar CFADs as good or better than the
1178 previous 3ICE versions, but peak reflectivity profiles for the moderate case were actually
1179 superior to the 3ICE in overall intensity despite the addition of a frozen drops/hail
1180 category by realistically decreasing monotonically with height above the freezing level as
1181 observed due to the greater fall speeds, which allowed higher density precipitation ice to
1182 remain near the freezing level.

1183

1184 *(A.4) Additional modifications to the 4ICE scheme*

1185 Several additional modifications have now been added to further improve the
1186 flexibility and performance of the 4ICE scheme. First, ice supersaturations on the order
1187 of tens of percent are commonly observed [Jensen et al., 2001; Stith et al., 2002; Garrett
1188 et al., 2005]; however, average ice supersaturations are much lower. The peak ice

1189 supersaturation was increased to allow up to 20% in the 4ICE scheme but was applied
1190 everywhere, resulting in a weaker convective system overall. The new formulation
1191 allows for a background supersaturation of 5%, which increases linearly up to a
1192 maximum of 21% as the updraft intensity increases above a background value of 2 m/s.
1193 Second, the autoconversion of cloud ice to snow (P_{saut}) follows a Kessler formulation
1194 where a threshold amount (i.e., of ice) must be exceeded before the excess is converted to
1195 in this case snow based on a specified timescale and efficiency. The previous
1196 configuration for P_{saut} was quite weak and although strengthened in 4ICE still appeared
1197 too weak and contributes to having a patchy anvil. Lowering the threshold from 0.6 g m^{-3}
1198 to 0.06 g m^{-3} improves the homogeneity of the simulated anvils. The Meyers *et al.*
1199 [1992] curve for the number of active IN was replaced by the Cooper curve [Cooper,
1200 1986]. Being a single moment scheme, the previous ice number concentration is not
1201 stored, which, using the Meyers curve, results in the number of IN decreasing as excess
1202 vapor is absorbed. In conjunction with this change, the IN number concentration is
1203 constrained such that the mean ice particle size cannot exceed the specified minimum
1204 snow size (i.e., 100 microns).

1205 Next, the snow mapping scheme was reconfigured to account for the effects of
1206 snow breakup via interactions with graupel and hail. Although dry collection is turned
1207 off in 4ICE such that graupel and hail do not collect snow, their interaction can affect the
1208 distribution of snow particle sizes. Over the years a lot of effort [e.g., Hallett and
1209 Mossop, 1974; Hobb and Rangno, 1985; Oraltay and Hallett, 1989] has been devoted to
1210 explaining the mechanisms by which ice crystal concentrations can be observed well in
1211 excess of the background IN concentration [e.g., Mossop et al., 1968, 1972; Hobbs, 1969,

1212 1974]. These secondary ice multiplication studies have focused primarily on the
1213 enhancement of ice crystal concentrations. Less research has been done in the area of
1214 mechanical ice breakup via ice-ice collisions [Yano and Phillips, 2011] and very little
1215 regarding the impact on the larger parent particles. In addition to the potential for
1216 interactions between various sizes of snow particles themselves to produce a self-limiting
1217 snow size distribution [Lo and Passarelli, 1982], larger aggregates are unlikely to coexist
1218 with faster falling graupel or hail particles as they would likely breakup as a result of
1219 such collisions. Vardiman [1978] performed early laboratory measurements of ice
1220 fragmentation and demonstrated the potential efficacy of mechanical fracturing especially
1221 of rimed dendrites by graupel. Griggs and Choulaton [1986] also conducted a laboratory
1222 study on ice fragmentation and reported that vapor-grown dendrites are fragile and that
1223 their collision with graupel could produce a substantial number of ice crystals.

1224 Using the laboratory data of Takahashi et al. [1995], Yano and Phillips [2011]
1225 constructed an idealized model to demonstrate that mechanical break up due to ice-ice
1226 collisions involving graupel can substantially contribute to the ice multiplication effect.
1227 Though these studies again focused on the production of ice fragments, it is apparent that
1228 such collisions would have an impact on the parent snow particle sizes. The snow
1229 mapping scheme that was carried over and modified in the 4ICE scheme has been further
1230 modified to allow a more robust aggregation effect in the absence of graupel and hail.
1231 However, when graupel and/or hail are present, a simple scaling (S_{hg}) based on the local
1232 graupel/hail mixing ratio(s) is used to increase the snow intercept obtained from the
1233 mapping scheme to reduce snow particle size where:

1234

1235 $S_{hgx} = \max(1, q_h \times 125.) + \max(1, q_g \times 25.)$ when $q_h > 0.008 \text{ g m}^{-3}$, $q_g > 0.04 \text{ g m}^{-3}$

1236

1237 and q_h and q_g are the hail and graupel mixing ratios, respectively. This formulation
1238 produces convective snow sizes that remain small but allows anvil snow sizes to become
1239 large using a common snow mapping and thus improve the effective mapping in each
1240 region rather utilize a single compromise mapping for both.

1241 Finally, a simple hail-mapping scheme was introduced. Lang et al. [2014]
1242 demonstrated the performance of the 4ICE scheme for both moderate and intense
1243 convection; however, because the scheme still retained the use of a fixed intercept, a
1244 series of experiments was conducted for each case using different hail intercepts (i.e.,
1245 equivalent to smaller-, medium-, and larger-sized hail). It was found that smaller hail
1246 performed the best for the moderate case, while medium hail performed best for the
1247 intense. As noted in Lang et al. [2014], it is not optimal to have to choose the hail
1248 intercept for each case *a priori*. Therefore, a simple hail mapping scheme has been
1249 devised based on the peak hail profiles from the moderate and intense cases in the Lang
1250 *et al.* [2014] study. In the mapping, a starting intercept appropriate for smaller hail (i.e.,
1251 0.240 cm^{-4}) is scaled down (i.e., hail size increases) as hail mixing ratio increases beyond
1252 a minimum threshold. It then reaches a minimum value (i.e., 0.0048 cm^{-4}) upon reaching
1253 a maximum threshold beyond which it no longer changes. The two thresholds are shown
1254 as a function of the local (i.e., in cloud not environmental) temperature in Figure A1.

1255 Figures A2 and A3 show some of the differences between the original 4ICE
1256 scheme (Figure A2) in Lang *et al.* [2014] and the 4ICE scheme with the additional
1257 improvements made for this study (Figure A3). Both schemes feature erect leading edge

1258 convective cores, but the current scheme has more of a transition region between the
1259 erect core and the trailing stratiform are due to the snow break up effect. Its stratiform
1260 features are also more horizontally stratified due to the associated change in the snow
1261 mapping, which appears to better match the observed stratiform structure, which is also
1262 quite horizontally stratified. Figure A4 shows that the current 4ICE scheme has slightly
1263 better CFAD score at most levels.
1264

1265 LIST OF TABLES

1266 Table 1: Key papers using high-resolution numerical cloud models with bulk
1267 microphysics schemes to study the impact of microphysical schemes on
1268 precipitation. Model type (2D or 3D), microphysical scheme (one moment or
1269 multi-moment), resolution (km), number of vertical layers, time step
1270 (seconds), case and integration time (hours) are all listed. Papers with a “*”
1271 are used for comparison with the present study, papers with a “#” denote
1272 development of a new scheme, papers with a “\$” modify/improve existing
1273 schemes, papers with a “&” compare different schemes, and papers with a
1274 “%” indicate process (budget) studies. TCM3 stands for the “Tropical
1275 Cyclone Model with triple nested movable mesh”.

1276 Table 2 List of numerical experiments.

1277 Table 3 Total rainfall and its convective and stratiform components from observations
1278 and NU-WRF simulations for three different microphysical schemes.

1279 Table 4 Total rainfall coverage (for rain rates greater than the Q2 minimum of 0.15
1280 mm/h) and its convective and stratiform components from observations and
1281 NU-WRF simulations for three different microphysical schemes.

1282 Table 5 Domain averaged hydrometeor mixing ratios for three different microphysics
1283 schemes, units in mm.

1284 Table 6 Domain averaged hydrometeor mixing ratios in the convective region for
1285 three different microphysics schemes, units in mm.

1286 Table 7 Domain averaged hydrometeor mixing ratios in the stratiform region for three
1287 different microphysics schemes, units in mm.

1288 Table 8 Domain averaged hydrometeor mixing ratios in the cloudy (but not
1289 convective or stratiform) region for three different microphysics schemes,
1290 units in mm.

1291

1292

	<i>Model</i>	<i>Microphysics</i>	<i>Resolutions</i> <i>Vertical Layers</i>	<i>Integration</i> <i>Time</i>	<i>Case</i>
Lin <i>et al.</i> (1983)	2D	3-ICE	200 m/95	48 min	Montana Hail Event
Cotton <i>et al.</i> (1982, 1986)	2D	3-ICE & Ni	500 m/31	5 hours	Orographic Snow
Rutledge and Hobbs (1984)	2D kinematic	3-ICE	600 m/20	Steady State	Narrow Cold Front
Lord <i>et al.</i> (1984) *	2D axisymmetric	3-ICE vs Warm Rain	2 km/20	4.5 days	Idealized
Yoshizaki (1986)#	2D slab-symmetric	3-ICE scheme vs Warm Rain	0.5 km/32	4.5 hours	12 September GATE Squall Line
Nicholls (1987)	2D slab-symmetric	3-ICE vs Warm Rain	0.5 km/25	5 hours	12 September GATE Squall Line
Fovell and Ogura (1988)#%	2D slab-symmetric	3-ICE vs Warm Rain	1 km/31	10 hours	Mid-latitude Squall Line
Tao and Simpson (1989, 1993)#	2D and 3D	3-ICE vs Warm Rain	1 km/31	12 hours	GATE Squall Line
Tao <i>et al.</i> (1990)	2D	3-ICE	1 km/31	12 hours	GATE Squall Line
McCumber <i>et al.</i> (1991)%\$	2D and 3D	3-ICE scheme (graupel vs hail, 2ICE vs 3ICE)	1 km/31	12 hours	GATE Squall Line
Wu <i>et al.</i> (1999)	2D slab-symmetric	2 ICE	3 km/52	39 days	TOGA COARE
Ferrier (1994), Ferrier <i>et al.</i> (1995)#	2D slab-symmetric	2-moment 4-ICE	1 km/31	12 hours	COHMEX, GATE Squall Line
Tao <i>et al.</i> (1995)	2D slab-symmetric	3-ICE	0.75 and 1 km/31	12 hours	EMEX, PRESTORM
Walko <i>et al.</i> (1995)#	2D	4-ICE	0.3 km/80	30 min	Idealized
Meyers <i>et al.</i> (1997)#\$	2D	2-moment 4-ICE	0.5 km/80	30 min	Idealized
Straka and Mansell (2005)#	3D	10-ICE	0.5 km/30	~2 hours	Idealized
Lang <i>et al.</i> (2007)\$	3D	3-ICE	0.25 to 1km /41	8 hours	LBA

Zeng <i>et al.</i> (2008)\$	2D and 3D	3-ICE	1 km/41	40 days	SCSMEX, KWAJEX
Milbrandt and Yau (2005)#	1D	Three-moment	/51	50 minutes	Idealized Hail Storm
Morrison <i>et al.</i> (2005)#	Single column model	Two moments and 2-ICE	Single column model 27 layers	3 days	SHEBA FIRE-FACE
Morrison and Grabowski (2008)#	2D	Two-moment ICE	50 m/60	90 minutes	Idealized
Reisner <i>et al.</i> (1998)#	MM5 Non-hydrostatic	3-ICE and 2- moment for ICE	2.2 km/27	6 hours (2.2 km grid)	Winter Storms
Thompson <i>et al.</i> (2004)#	MM5 2D	3-ICE	10 km/39	3 hours	Idealized
Thompson <i>et al.</i> (2008)\$	WRF 2D	3-ICE	10 km/39	6 hours	Idealized
Colle and Mass (2000)	MM5 Non-hydrostatic	3-ICE	1.33 km/38	96 hours	Orographic Flooding
Colle and Zeng (2004)%	2-D MM5 Non-hydrostatic	3-ICE	1.33 km/39	12 hours	Orographic
Colle <i>et al.</i> (2005)%	MM5 Non-hydrostatic	3-ICE	1.33 km/320	36 hours	IMPROVE
Yang and Ching (2005)*	MM5 Non-hydrostatic	3-ICE	6.67 km/23	2.5 days	Typhoon Toraji (2001)
Zhu and Zhang (2006b)*	MM5 Non-hydrostatic	3-ICE	4 km/24	5 days	Bonnie (1998)
Wang (2002)*	TCM3-hydrostatic	3-ICE	5 km/21	5 days	Idealized
Hong <i>et al.</i> (2004)#	WRF Non-hydrostatic	3-ICE	45 km/23	48 hours	Korean Heavy Rainfall event
Li and Pu (2008)*	WRF Non-hydrostatic	2-ICE and 3-ICE	3 km/31	1.25 days	Hurricane Emily (2005)
Jankov <i>et al.</i> (2005; 2007)*	WRF Non-hydrostatic	2-ICE and 3ICE	12 km/31	1 day	IHOP
Dudhia <i>et al.</i> (2008)***	WRF Non-hydrostatic	3-ICE	5 km/31	1.5 days	Korean Heavy Snow event
Tao <i>et al.</i> (2009, 2011)	WRF Non-hydrostatic	2-ICE and 3ICE 3ICE and 4ICE	1 km/41 1.667 km/31	1.5 days 3 days	IHOP and Hurricane Katrina (2005)

Han <i>et al.</i> (2012)&	WRF Non-hydrostatic	1- and 2-moment for 3ICE	1.3 km/52	2 days	Winter cyclone in northern california
Iguchi <i>et al.</i> (2012a,b)	WRF Non-hydrostatic	SBM for 4ICE	1 km/60	36 h	C3VP and MC3E
Li <i>et al.</i> (2009a,b)&	2D	Bulk and SBM	1 km/33	12 h	PRE-STORM
Del Genio <i>et al.</i> (2012)	WRF Non-hydrostatic	2-moment for 3ICE	600 m/50	3 days	TWP-ICE
Gilmore <i>et al.</i> (2004)\$	SAM	1-moment for 3ICE	1 km/ 40	2 h	Idealized
Hong <i>et al.</i> (2003)#	WRF Non-hydrostatic	1-moment for 3ICE	2D: 250 m/ 80 3D: 45 km/23	2D: 1 h 3D: 2 days	2D Idealized 3D
Powell <i>et al.</i> (2012)&	WRF Non-hydrostatic	1- and 2-moment for 3ICE	3 km/61	24h and 30h	AMMA
Tao <i>et al.</i> (2013)\$	WRF Non-hydrostatic	3ICE	2 km/ 41	2 days	MC3E
Wu <i>et al.</i> (2013)&	WRF Non-hydrostatic	2-ICE and 3ICE	3 km/ 41	2 days	SGP MCSs
Lang <i>et al.</i> (2011)\$	GCE 3D	3ICE	250, 500 m/70	1 day and 72 h	TRMM LBA and KWAJEX
Morrison <i>et al.</i> (2008)&	WRF 2D	1- and 2-moment for 3ICE	250 m/?	7 h	Idealized
Varble <i>et al.</i> (2011)&	DHARMA, UKMO, MESONH, SAM	1- and 2-moment for 3ICE	917 m and 1 km/ 50 or 120	16 days	TWP-ICE
Fridlind <i>et al.</i> (2012)&	Multi-models	1- and 2-moment for 2ICE or 3ICE	900m-3km/100- 1000m	6 days	TWP-ICE
Van Weverberg <i>et al.</i> (2012)\$	ARPS	1-moment 3ICE	3km/50	30 h	Convective and stratiform cases
Van Weverberg <i>et al.</i> (2012)&	WRF 2D	2-moment for 3ICE, 4ICE	1 km/ 250m 1 km/40	5 h	Idealized
Van Weverberg <i>et al.</i> (2013a,b)	WRF 3D	2-moment for 3ICE	1km/40	5h	Idealized and TWP
Van Weverberg <i>et al.</i> (2013)&	WRF Non-hydrostatic	1- and 2-moment for 2ICE or 3ICE	4km/35	7 days	TWP
Bryan and Morrison	CM1	1- and 2-moment	250m/100	9 h	Idealized

(2011)&	3D	for 3ICE			
Morrison and Milbrandt (2011)&	WRF 3D	2- moment for 3ICE and 4ICE	1km/500m	2 h	Idealized
Morrison and Grabowski (2007)&	2D kinematic modeling framework	Bulk 2-moment and bin/warm rain	NAN	NAN	Idealized
Luo <i>et al.</i> (2010)\$&	WRF Non-hydrostatic	1- and 2-moment for 3ICE	3.3 km/30	1 day	Mei-Yu front
Li <i>et al.</i> (2008)	WRF 3D with 3DVAR	1-moment 3ICE	27, 9, 3 km/31	30 hours	Hurricane Emily
Molthan and Colle (2012)	WRF	1- and 2-moment 3ICE	9, 3, 1 km/34	1 case	C3VP synoptic snow
Guy <i>et al.</i> (2013)	GCE 3D	1-moment 3ICE	1 km / 63	2 cases	AMMA WAM/AEW Sahel
Lang <i>et al.</i> (2014)	GCE 3D	1-moment 3ICE and 4ICE	200 m – 1 km / 70 - 76	6 – 96 h	TRMM LBA and MC3E convection
Morrison and Milbrandt (2015)#	WRF 2D	1-moment Predicted particle properties or P3	1 km/80	6 h	Idealized
Morrison <i>et al.</i> (2015)&	WRF	P3 and 3ICE	1 km/100	6 h	Oklahoma squall line

1293

1294 Table 1 Key papers using high-resolution numerical cloud models with bulk microphysics
1295 schemes to study the impact of microphysical schemes on precipitation. Model type
1296 (2D or 3D), microphysical scheme (one moment or multi-moment), resolution (km),
1297 number of vertical layers, time step (seconds), case and integration time (hours) are all
1298 listed. Papers with a “*” are used for comparison with the present study, papers with a
1299 “#” denote development of a new scheme, papers with a “\$” modify/improve existing
1300 schemes, papers with a “&” compare different schemes, and papers with a “%” indicate
1301 process (budget) studies. TCM3 stands for the “Tropical Cyclone Model with triple
1302 nested movable mesh”.

1303

1304

Run	Microphysics
Graupel	As Tao et al. (2013) except for 1 km
Hail	1 km with 3ICE - hail option
4ICE	1 km with updated 4ICE

1305

1306 Table 2 List of numerical experiments.

1307

1308

1309

	Total Rainfall (mm)	Convective Rainfall (mm)	Stratiform Rainfall (mm)	Stratiform %
Observation	14.12	8.66	4.94	35.01
Graupel	9.31	3.86	4.90	52.65
Hail	9.38	5.59	3.27	34.87
4ICE	10.30	5.83	4.02	39.05

1310

1311 Table 3 Total rainfall and its convective and stratiform components from observations
1312 and NU-WRF simulations for three different microphysical schemes.

1313

1314

1315

1316

Run	Total Rainfall Area Coverage in %	Convective Area Coverage in %	Stratiform Aera Coverage in %
Observation	46.51	4.50	24.03
Graupel	25.09	5.01	15.39
Hail	25.64	4.40	13.68
4ICE	23.99	5.13	14.98

1317

1318 Table 4 Total rainfall coverage (for rain rates greater than the Q2 minimum of 0.15
1319 mm/h) and its convective and stratiform components from observations and
1320 NU-WRF simulations for three different microphysical schemes.

1321

	Cloud Water	Rain	Cloud Ice	Snow	Graupel	Hail
Graupel	0.218	0.288	0.534	1.439	0.706	N/A
Hail	0.198	0.222	0.099	0.810	N/A	0.155
4ICE	0.190	0.291	0.314	1.608	0.185	0.124

1322

1323 Table 5 Domain averaged hydrometeor mixing ratios for three different microphysics
 1324 schemes, units in mm.

1325

	Cloud Water	Rain	Cloud Ice	Snow	Graupel	Hail
Graupel	0.076	0.151	0.108	0.273	0.240	N/A
Hail	0.063	0.159	0.027	0.161	N/A	0.117
4ICE	0.075	0.186	0.100	0.284	0.067	0.101

1326

1327 Table 6 Domain averaged hydrometeor mixing ratios in the convective region for
 1328 three different microphysics schemes, units in mm.

1329

1330

1331

1332

1333

	Cloud Water	Rain	Cloud Ice	Snow	Graupel	Hail
Graupel	0.058	0.133	0.197	0.823	0.388	N/A
Hail	0.048	0.059	0.032	0.529	N/A	0.036
4ICE	0.042	0.101	0.120	0.982	0.100	0.021

1334

1335 Table 7 Domain averaged hydrometeor mixing ratios in the stratiform region for three
 1336 different microphysics schemes, units in mm.

	Cloud Water	Rain	Cloud Ice	Snow	Graupel	Hail
Graupel	0.084	0.004	0.229	0.343	0.078	N/A
Hail	0.087	0.004	0.040	0.120	N/A	0.002
4ICE	0.073	0.004	0.094	0.342	0.018	0.002

1337

1338 Table 8 Domain averaged hydrometeor mixing ratios in the cloudy (but not
 1339 convective or stratiform) region for three different microphysics schemes,
 1340 units in mm.

1341

1342 LIST OF FIGURES

1343 Figure 1 NU-WRF grid configuration. The outer domain (labeled 1 at the center) has a
1344 horizontal resolution of 9 km. The middle domain (labeled 2) has a horizontal
1345 resolution of 3 km, and the inner domain (labeled 3) has a horizontal resolution
1346 of 1 km and covers the southern Plains.

1347 Figure 2 Surface one hour accumulated rainfall from (a) Q2 radar-only and the (b)
1348 Graupel, (c) Hail, and (d) 4ICE NU-WRF simulations ending at 10 UTC on 20
1349 May 2011. The precipitation analysis area is indicated by the red boundary.

1350 Figure 3 Observed and NU-WRF simulated convective and stratiform areas at 10 UTC
1351 on 20 May 2011. Red indicates convective regions and green stratiform
1352 regions.

1353 Figure 4 PDFs (probability distribution functions) of observed and NU-WRF simulated
1354 rainfall intensity in mm h^{-1} from three different microphysical schemes. The
1355 observed rain rates are from Q2. PDFs were calculated every 10 minutes from
1356 both observed and simulated datasets from 06 UTC to 12 UTC on 20 May
1357 2011 within the analysis domains shown in Figure 2.

1358 Figure 5 Hydrometeor profiles from the (a) Graupel, (b) Hail, and (c) 4ICE schemes
1359 from 06 UTC to 12 UTC on 20 May 2011.

1360 Figure 6 Same as Figure 5 except for the convective regions.

1361 Figure 7 Same as Figure 5 except for the stratiform regions.

1362 Figure 8 Maximum radar reflectivities for (a) NEXRAD observations and NU-WRF
1363 simulations with the (b) Graupel, (c) Hail, (d) 4ICE microphysics schemes.

1364 Right axes are heights in km, while horizontal lines show the time range from
1365 00 UTC to 12 UTC on 20 May 2011.

1366 Figure 9 Radar reflectivity CFADs from (a) NEXRAD observations and NU-WRF
1367 simulations with the (b) Graupel, (c) Hail, (d) 4ICE microphysics schemes from
1368 00 UTC to 06 UTC on 20 May 2011. Right axes are heights in km; horizontal
1369 dashed lines indicate the level of the 0 °C environmental temperature.

1370 Figure 10 PDF matching scores for the CFADs in Figure 9. The score indicates the
1371 amount of overlap between the simulated and observed PDF at each level.

1372 Figure 11 Components of the 4ICE radar reflectivity CFAD shown in Figure 9 (d) due
1373 to (a) rain, (b) snow, (c) graupel and (d) hail. Horizontal dashed lines indicate
1374 the level of the 0 °C environmental temperature.

1375 Figure 12 Vertical cross-section of NEXRAD radar reflectivity at 10 UTC on 20 May
1376 2011. Positions of the cross-sections are shown by the lines in Figure 2 for
1377 the radar observations and WRF simulations, respectively.

1378 Figure 13 Top panel same as Figure 12, but for the NU-WRF Graupel simulation.
1379 Bottom panel shows the concurrent NU-WRF vertical velocity (colored
1380 contours), equivalent potential temperature (black contours), and virtual
1381 potential temperature (filled contours).

1382 Figure 14 Same as Figure 13 but for the NU-WRF Hail simulation.

1383 Figure 15 Same as Figure 13 but for the NU-WRF 4ICE simulation.

1384 Figure 16 Vertical velocity CFADs of in-cloud up- and downdrafts in the total,
1385 convective and stratiform regions.

1386 Figure A1 Hail mapping size thresholds as a function of hail mixing ratio and local in

1387 cloud temperature. Hail mixing ratios less than the dashed line use a larger
1388 intercept (i.e., 0.240 cm^{-4}) representative of smaller hail while those greater than
1389 the solid line use a smaller intercept (i.e., 0.0048 cm^{-4}) representative of larger
1390 hail at each given temperature. Intercept values are interpolated for mixing
1391 ratios between the two thresholds.

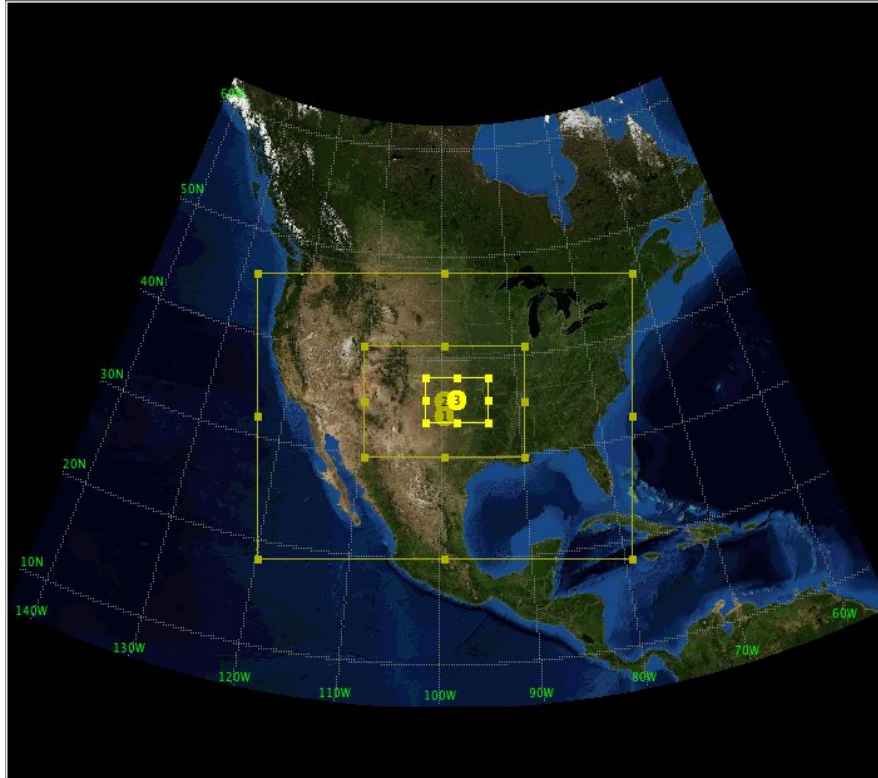
1392 Figure A2 Same as the top panel in Figure 15 except for the previous 4ICE scheme
1393 [Lang et al. 2014]. Horizontal composite reflectivity and stratiform separation
1394 are shown in the top two panels.

1395 Figure A3 Same as Figure A2 but for the current 4ICE scheme.

1396 Figure A4 Same as Figure 10 except with the previous 4ICE scheme [4ICE_v0, Lang et
1397 al., 2014] added.

1398

1399



1400

1401

1402 Figure 2 NU-WRF grid configuration. The outer domain (labeled 1 at the center) has a
1403 horizontal resolution of 9 km. The middle domain (labeled 2) has a horizontal
1404 resolution of 3 km, and the inner domain (labeled 3) has a horizontal resolution
1405 of 1 km and covers the southern Plains.

1406

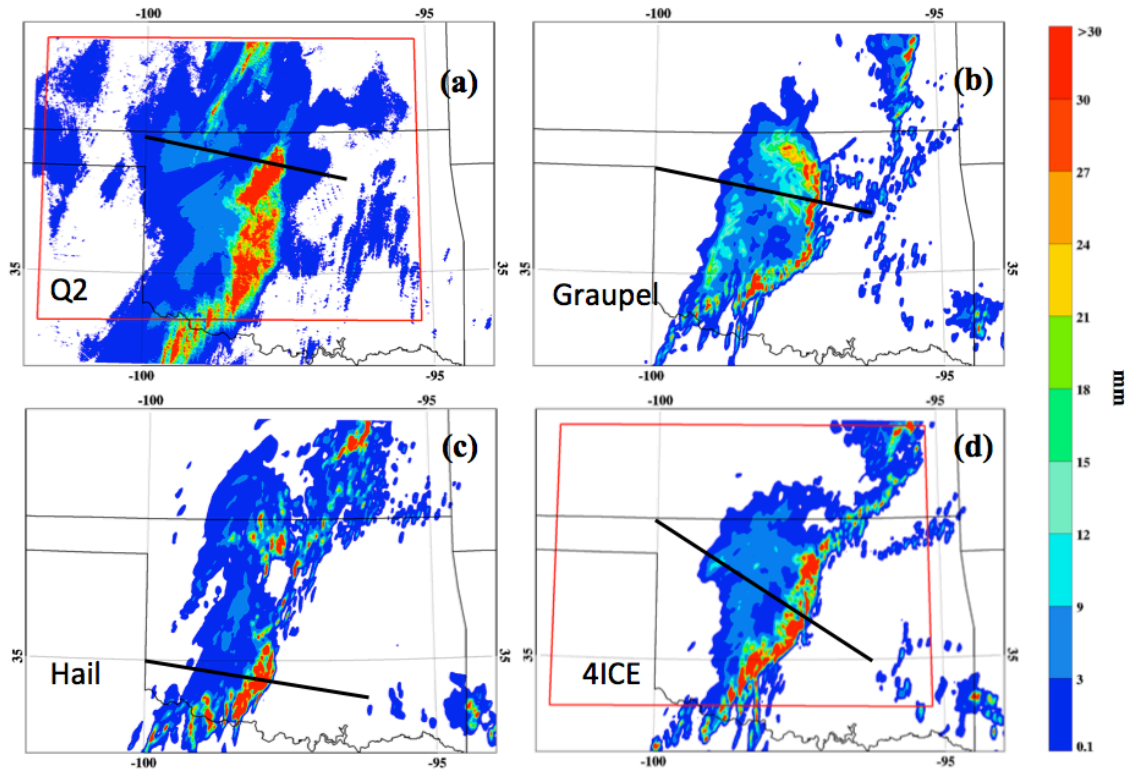
1407

1408

1409

1410

1411



1412

1413 Figure 2 Surface one hour accumulated rainfall from (a) Q2 radar-only and the (b)

1414

Graupel, (c) Hail, and (d) 4ICE NU-WRF simulations ending at 10 UTC on 20

1415

May 2011. The precipitation analysis area is indicated by the red boundary.

1416

1417

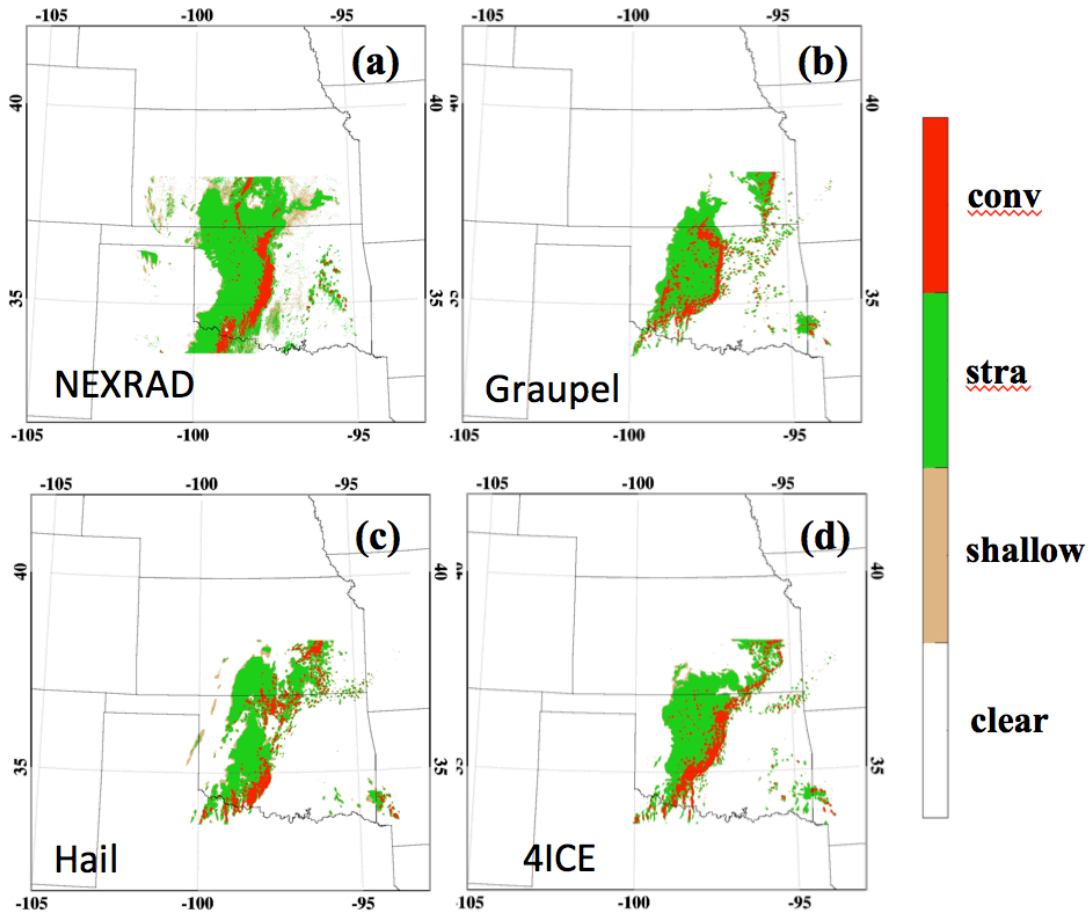
1418

1419

1420

1421

1422



1423

1424 Figure 3 Observed and NU-WRF simulated convective and stratiform areas at 10 UTC
 1425 on 20 May 2011. Red indicates convective regions and green stratiform
 1426 regions.

1427

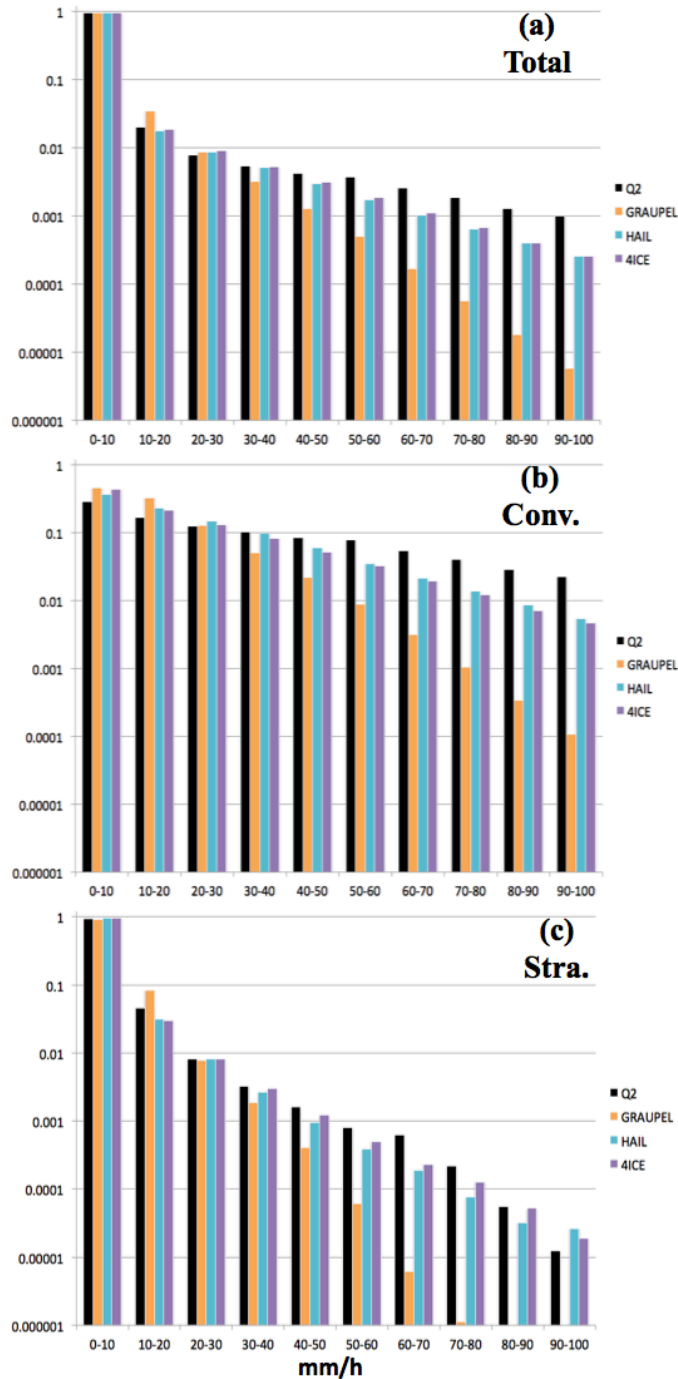
1428

1429

1430

1431

1432



1433

1434 Figure 4 PDFs (probability distribution functions) of observed and NU-WRF simulated
 1435 rainfall intensity in mm h⁻¹ from the three different Goddard microphysical
 1436 schemes for the (a) total, (b) convective, and (c) stratiform regions. The
 1437 observed rain rates are from Q2. PDFs were calculated every 10 minutes from

1438 both observed and simulated datasets from 06 UTC to 12 UTC on 20 May
1439 2011 within the analysis domains shown in Figure 2.

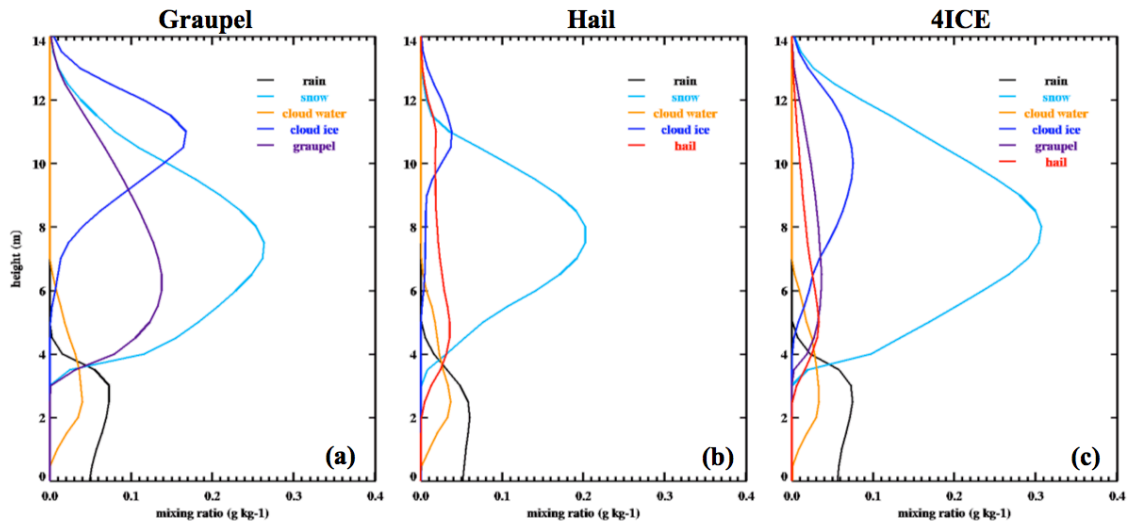
1440

1441

1442

1443

1444



1445

1446 Figure 5 Hydrometeor profiles from the (a) Graupel, (b) Hail, and (c) 4ICE schemes

1447

from 06 UTC to 12 UTC on 20 May 2011.

1448

1449

1450

1451

1452

1453

1454

1455

1456

1457

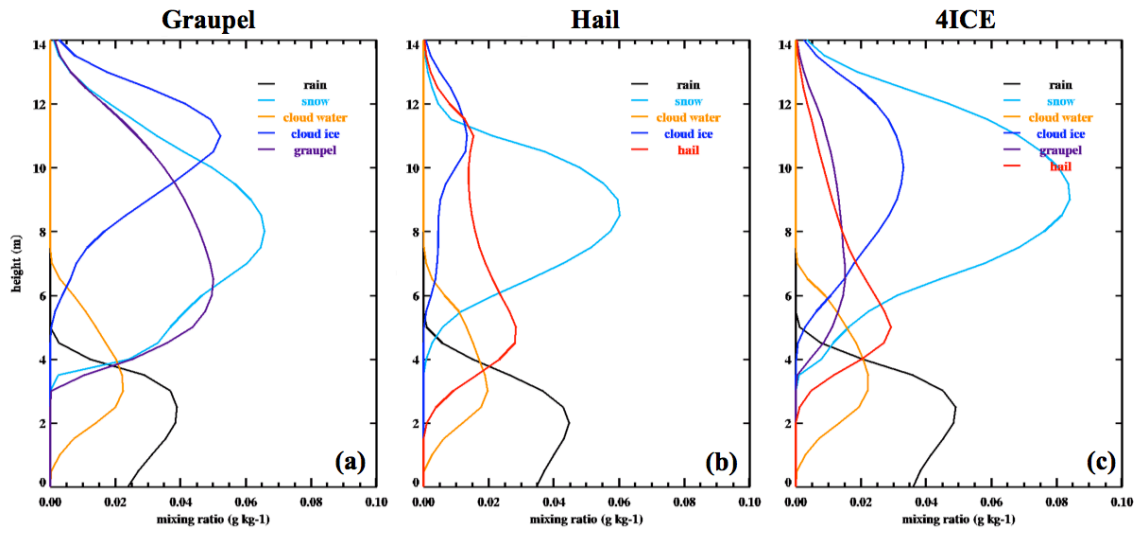
1458

1459

1460

1461

1462



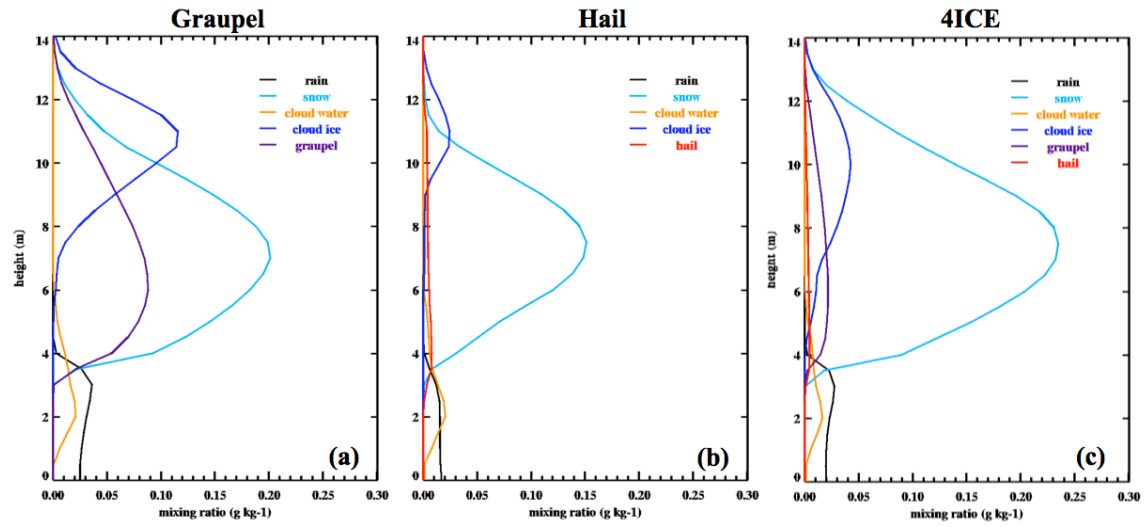
1463

1464 Figure 6 Same as Figure 5 except for the convective regions.

1465

1466

1467



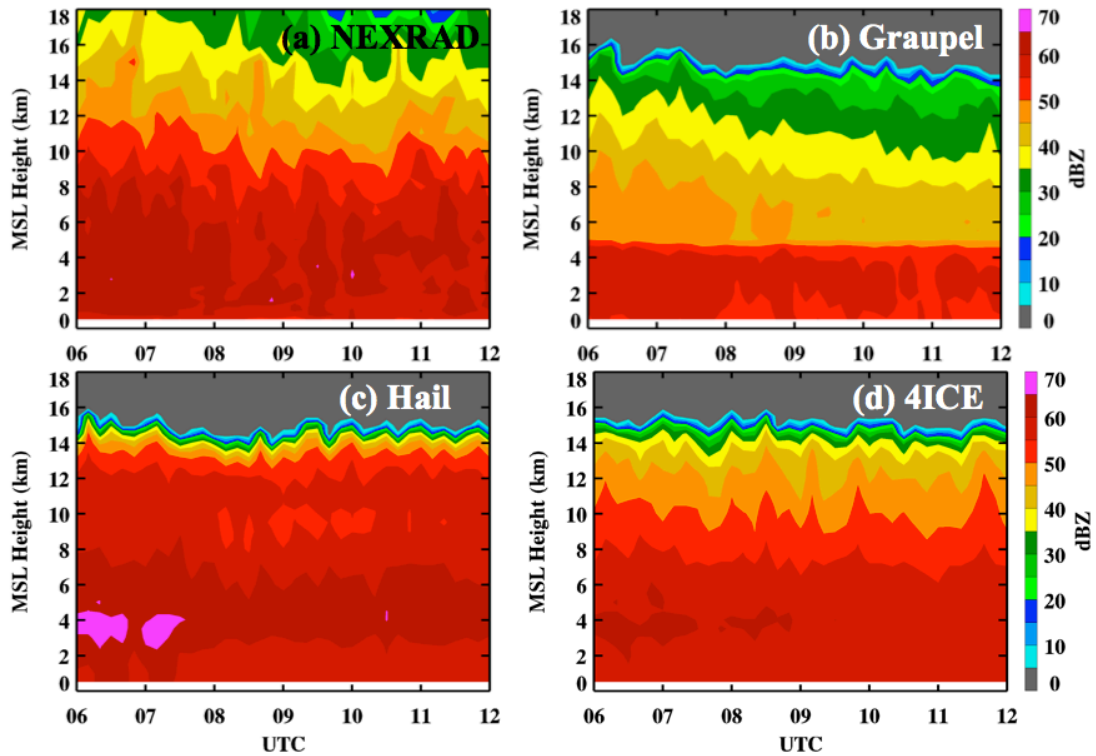
1468

1469 Figure 7 Same as Figure 5 except for the stratiform regions.

1470

1471

1472



1473

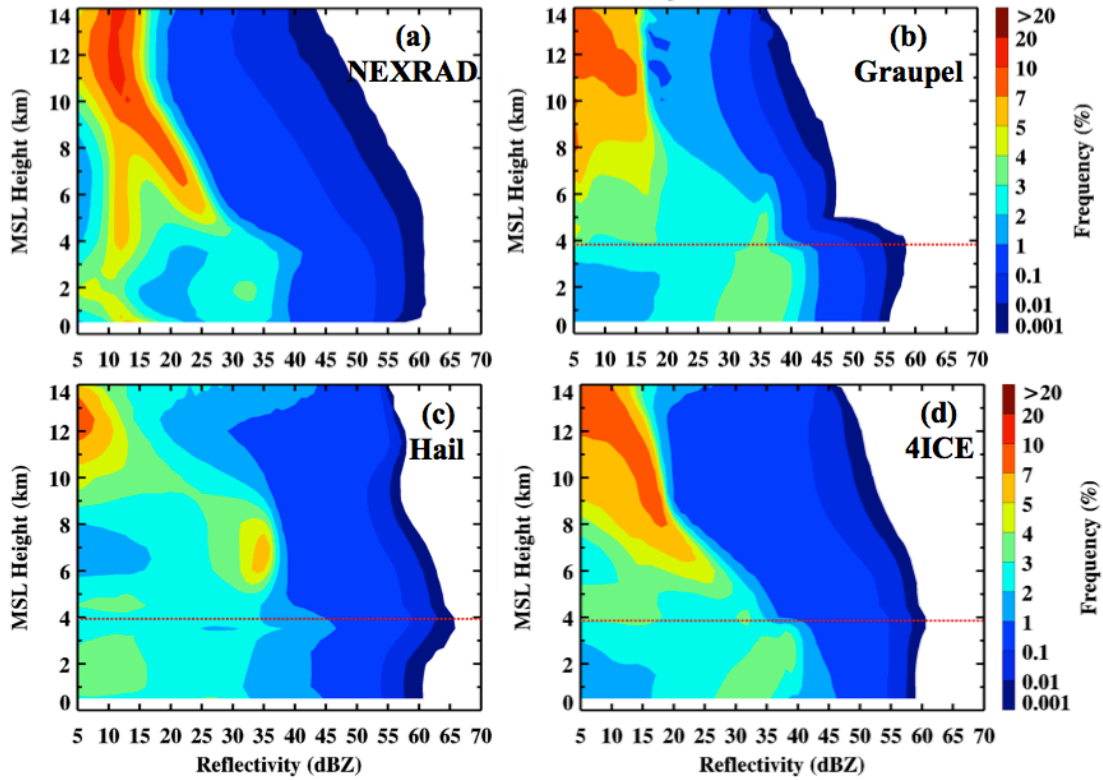
1474 Figure 8 Maximum radar reflectivities for (a) NEXRAD observations and NU-WRF
1475 simulations with the (b) Graupel, (c) Hail, (d) 4ICE microphysics schemes.
1476 Right axes are heights in km, while horizontal lines show the time range from
1477 00 UTC to 12 UTC on 20 May 2011.

1478

1479

1480

1481



1482

1483 Figure 9 Radar reflectivity CFADs from (a) NEXRAD observations and NU-WRF

1484 simulations with the (b) Graupel, (c) Hail, (d) 4ICE microphysics schemes from

1485 00 UTC to 06 UTC on 20 May 2011. Right axes are heights in km; horizontal

1486 dashed lines indicate the level of the 0 °C environmental temperature.

1487

1488

1489

1490

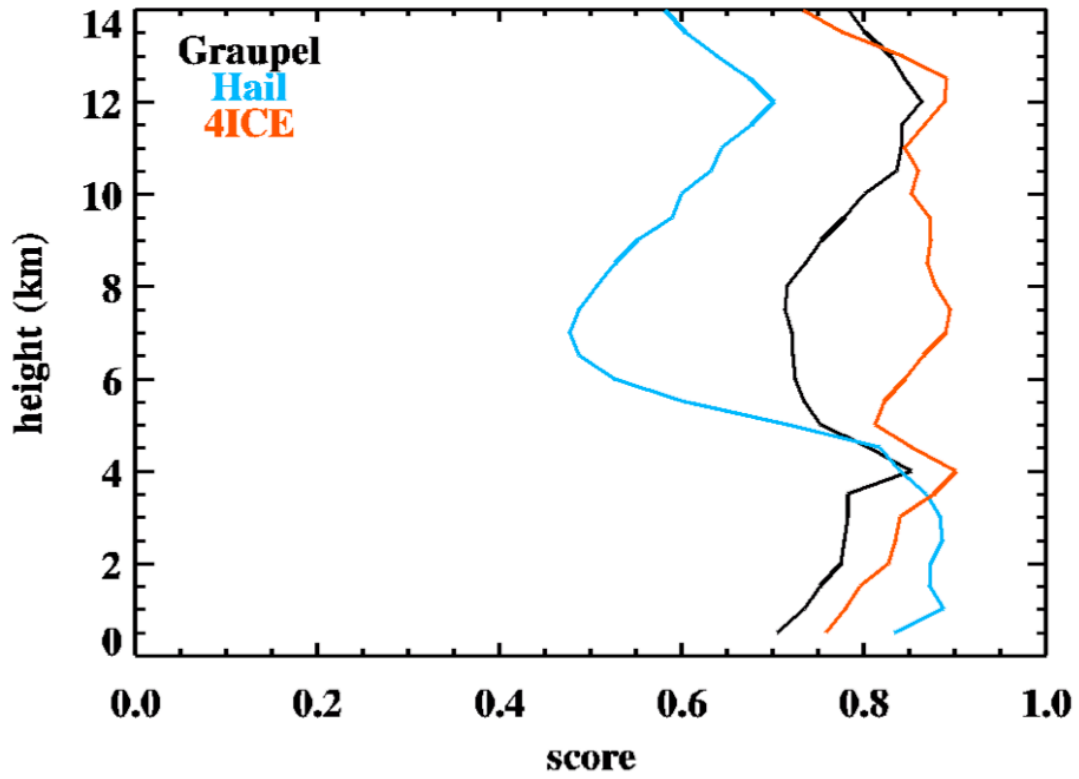
1491

1492

1493

1494

1495



1496

1497 Figure 10 PDF matching scores for the CFADs in Figure 9. The score indicates the
1498 amount of overlap between the simulated and observed PDF at each level.

1499

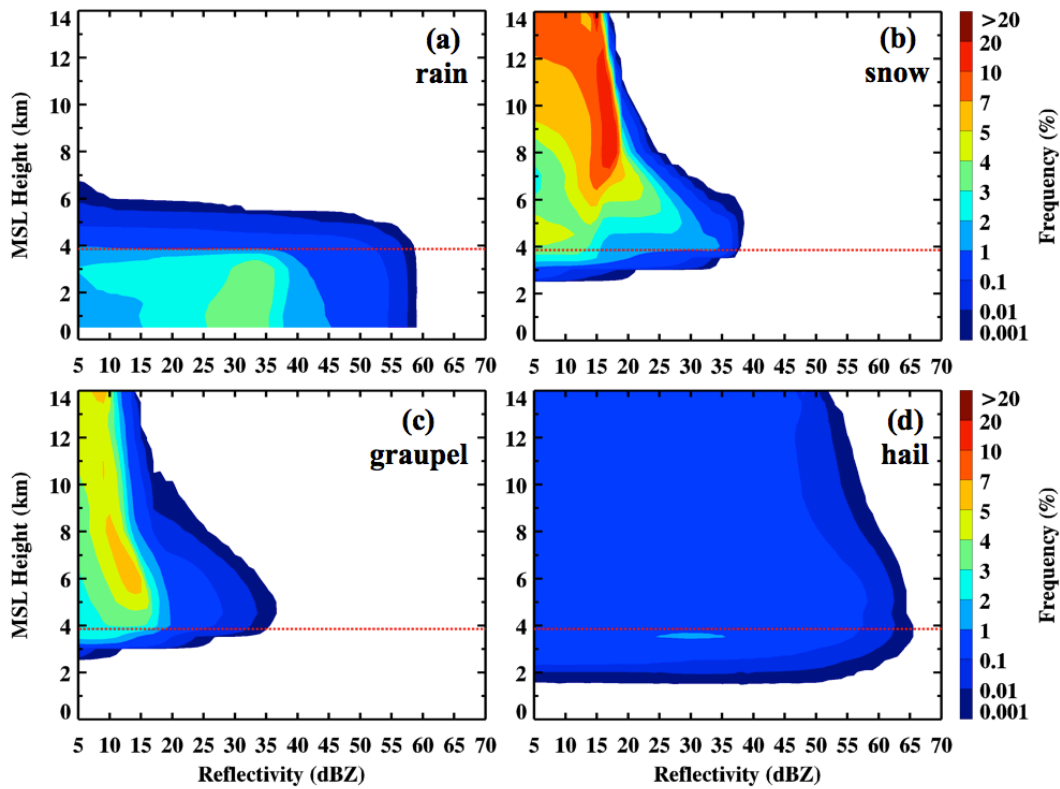
1500

1501

1502

1503

1504
1505
1506
1507
1508
1509

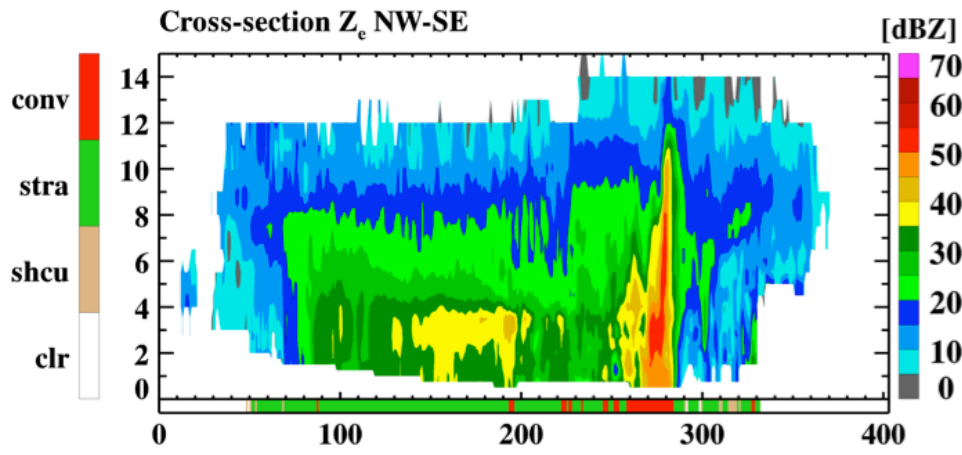


1510
1511
1512
1513
1514
1515
1516

Figure 11 Components of the 4ICE radar reflectivity CFAD shown in Figure 9 (d) due to (a) rain, (b) snow, (c) graupel and (d) hail. Horizontal dashed lines indicate the level of the 0 °C environmental temperature.

1517

1518



1519

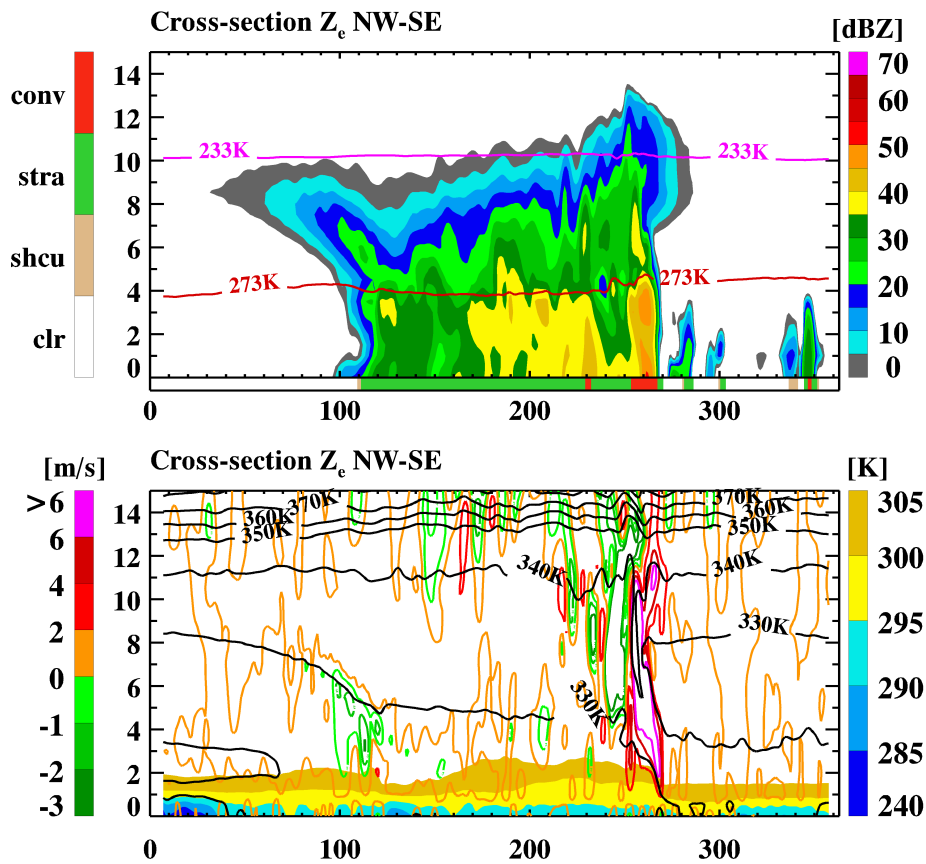
1520 Figure 12 Vertical cross-section of NEXRAD radar reflectivity at 10 UTC on 20 May

1521 2011. Positions of the cross-sections are shown by the lines in Figure 2 for

1522 the radar observations and WRF simulations, respectively.

1523

1524



1525

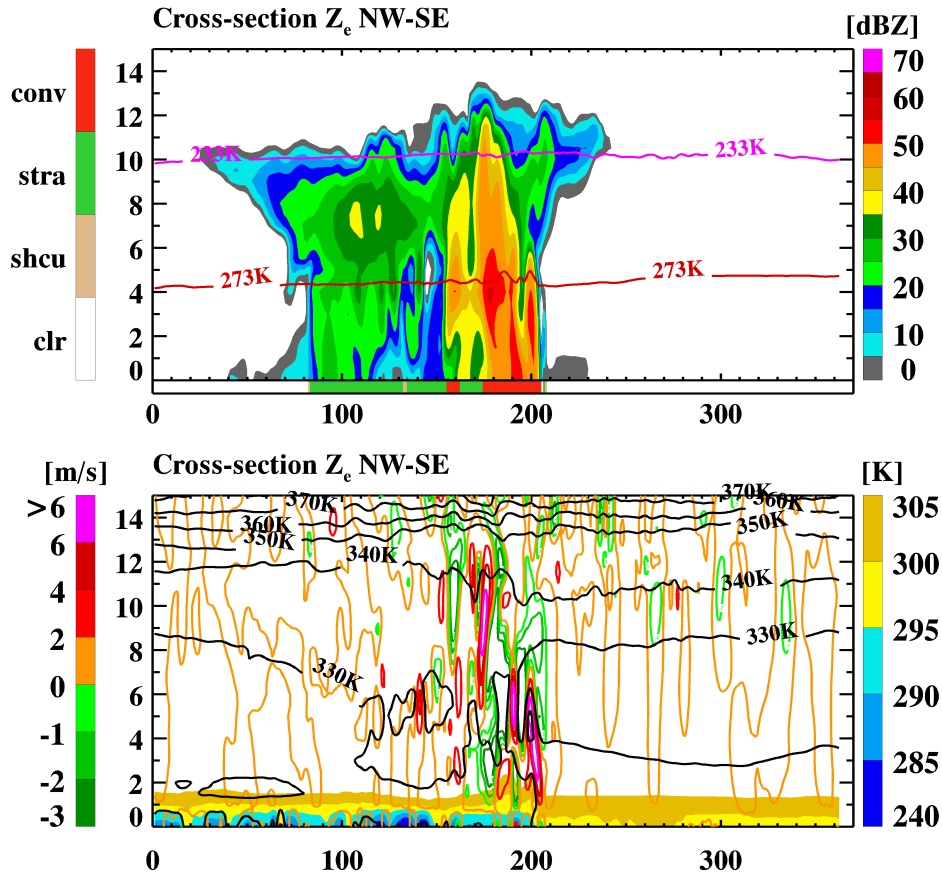
1526 Figure 13 Top panel same as Figure 12, but for the NU-WRF Graupel simulation.

1527 Bottom panel shows the concurrent NU-WRF vertical velocity (colored

1528 contours), equivalent potential temperature (black contours), and virtual

1529 potential temperature (filled contours).

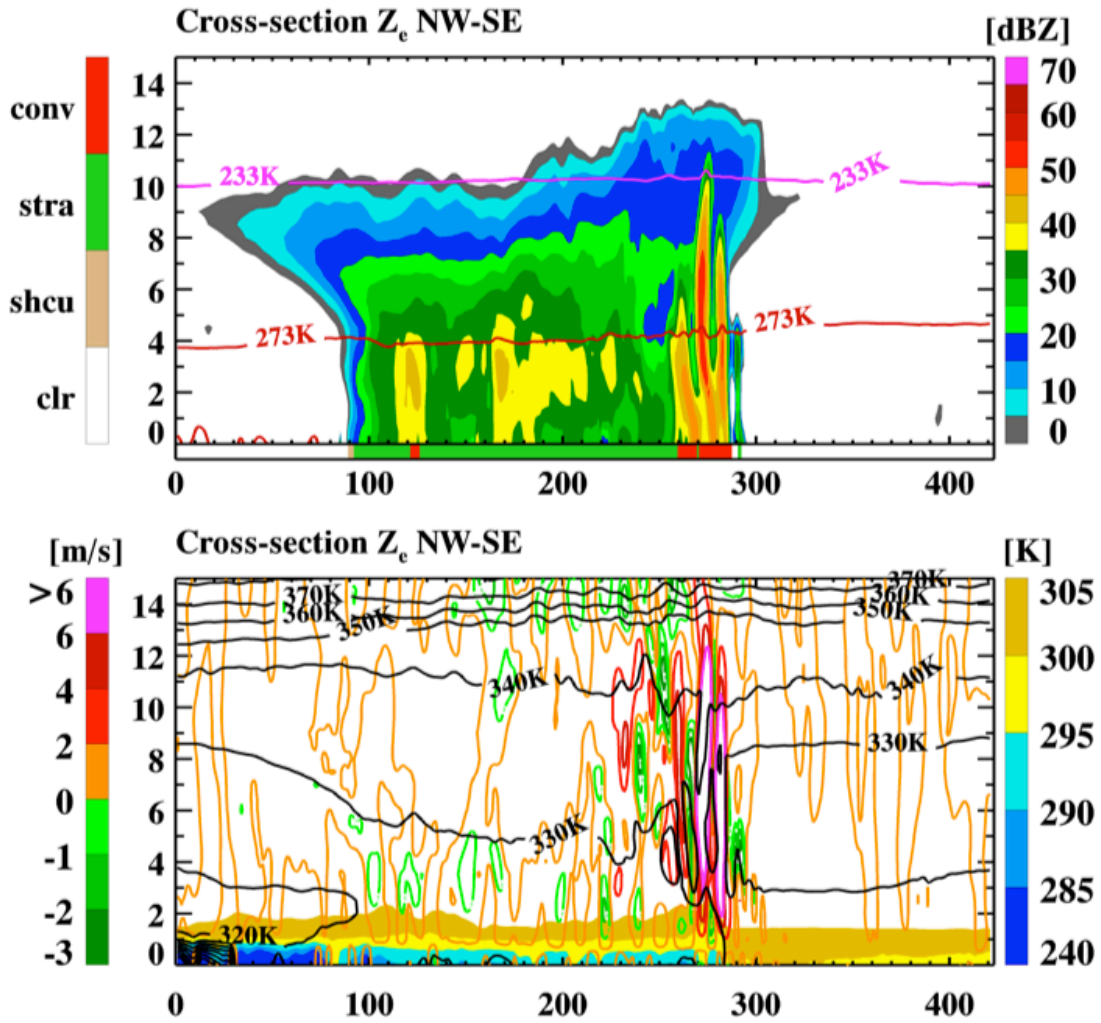
1530



1531

1532 Figure 14 Same as Figure 13 but for the NU-WRF Hail simulation.

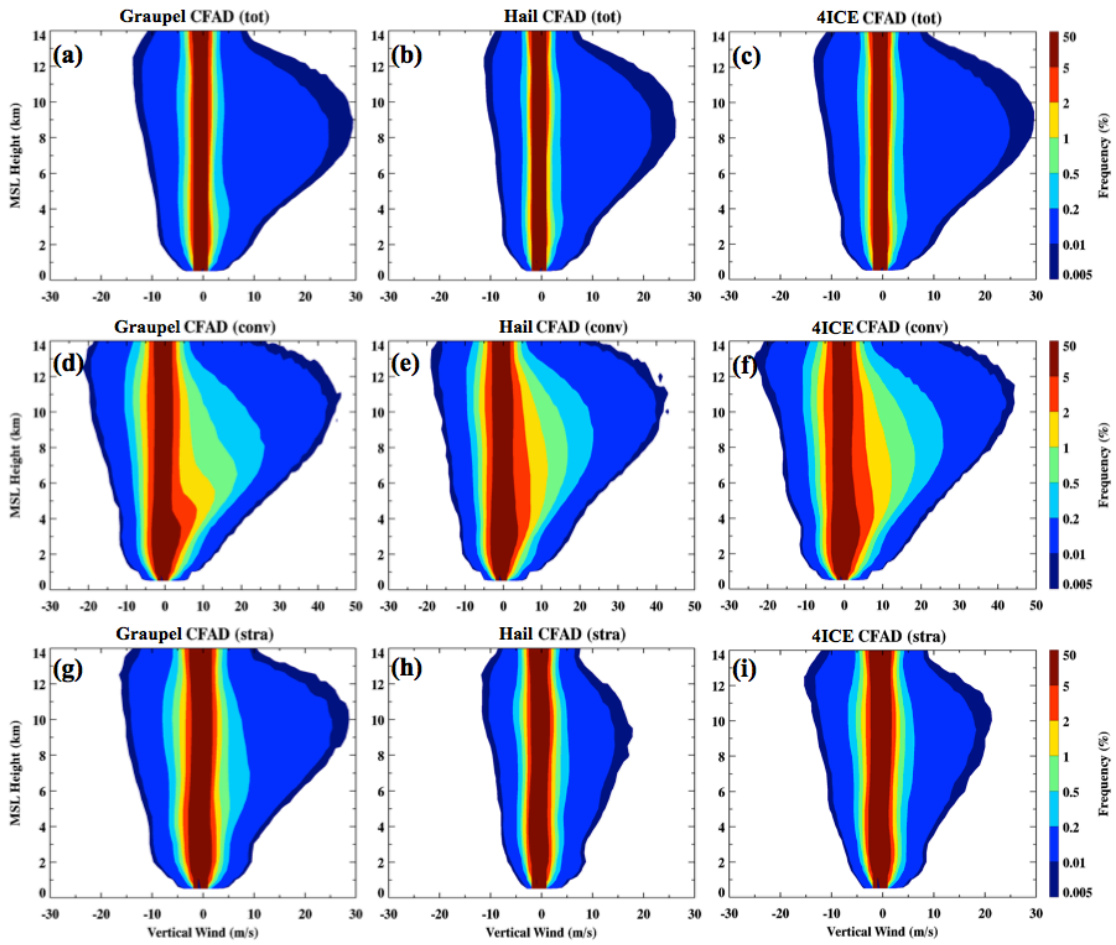
1533



1534

1535 Figure 15 Same as Figure 13 but for the NU-WRF 4ICE simulation.

1536



1537

1538 Figure 16 Vertical velocity CFADs of in-cloud up- and downdrafts in the total,
1539 convective and stratiform regions.

1540

1541

1542

1543

1544

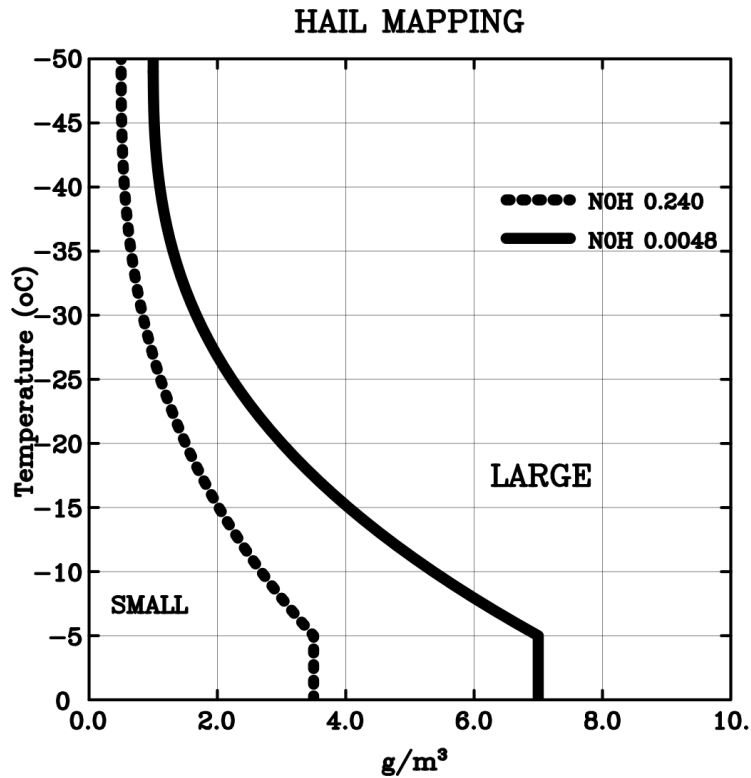
1545

1546

1547

1548

1549



1550

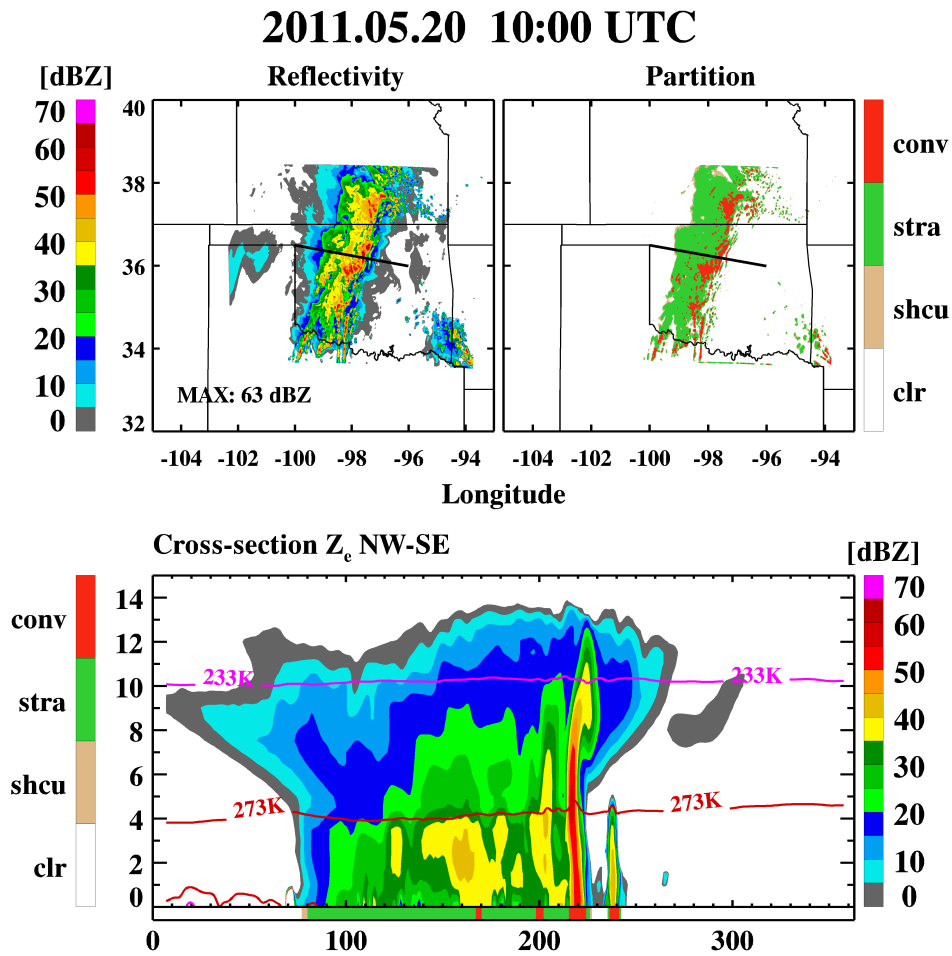
1551

1552

1553 Figure A1 Hail mapping size thresholds as a function of hail mixing ratio and local in
1554 cloud temperature. Hail mixing ratios less than the dashed line use a larger
1555 intercept (i.e., 0.240 cm^{-4}) representative of smaller hail while those greater than
1556 the solid line use a smaller intercept (i.e., 0.0048 cm^{-4}) representative of larger
1557 hail at each given temperature. Intercept values are interpolated for mixing
1558 ratios between the two thresholds.

1559

1560



1561

1562

1563 Figure A2 Same as the top panel in Figure 15 except for the previous 4ICE scheme

1564 [Lang et al. 2014]. Horizontal composite reflectivity and stratiform separation

1565 are shown in the top two panels.

1566

1567

1568

1569

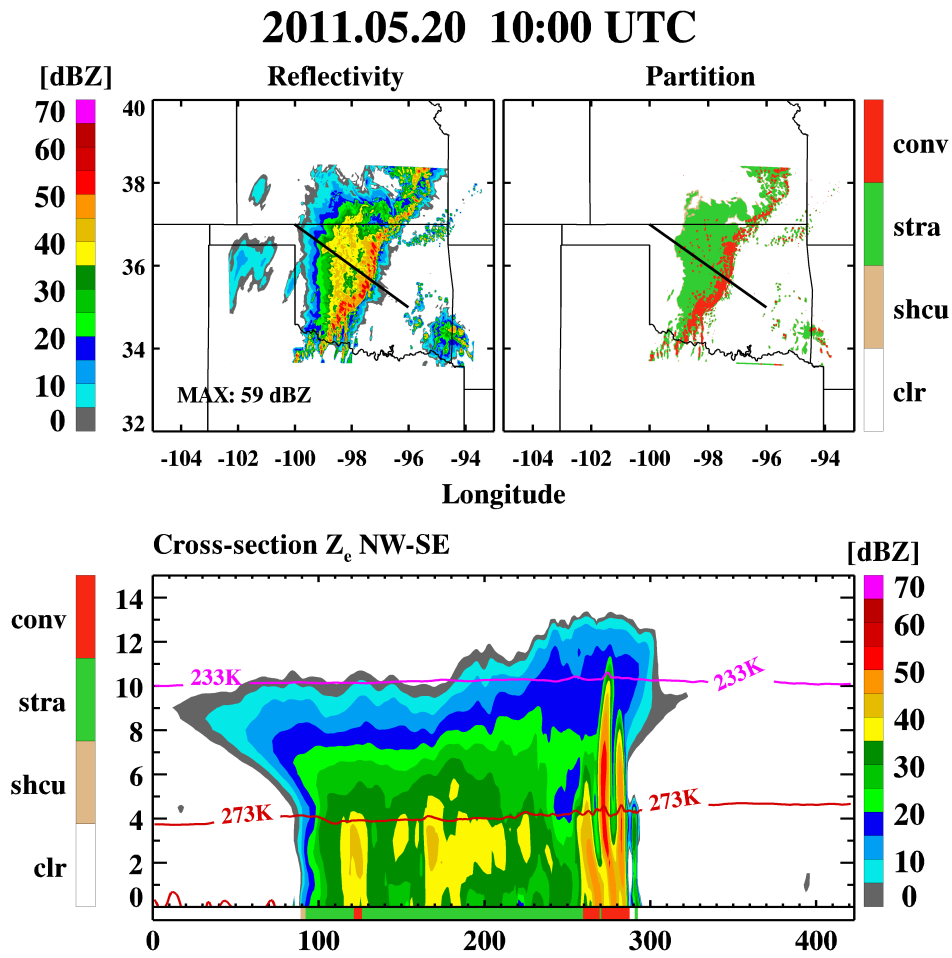
1570

1571

1572

1573

1574



1575

1576 Figure A3 Same as Figure A2 but for the current 4ICE scheme.

1577

1578

1579

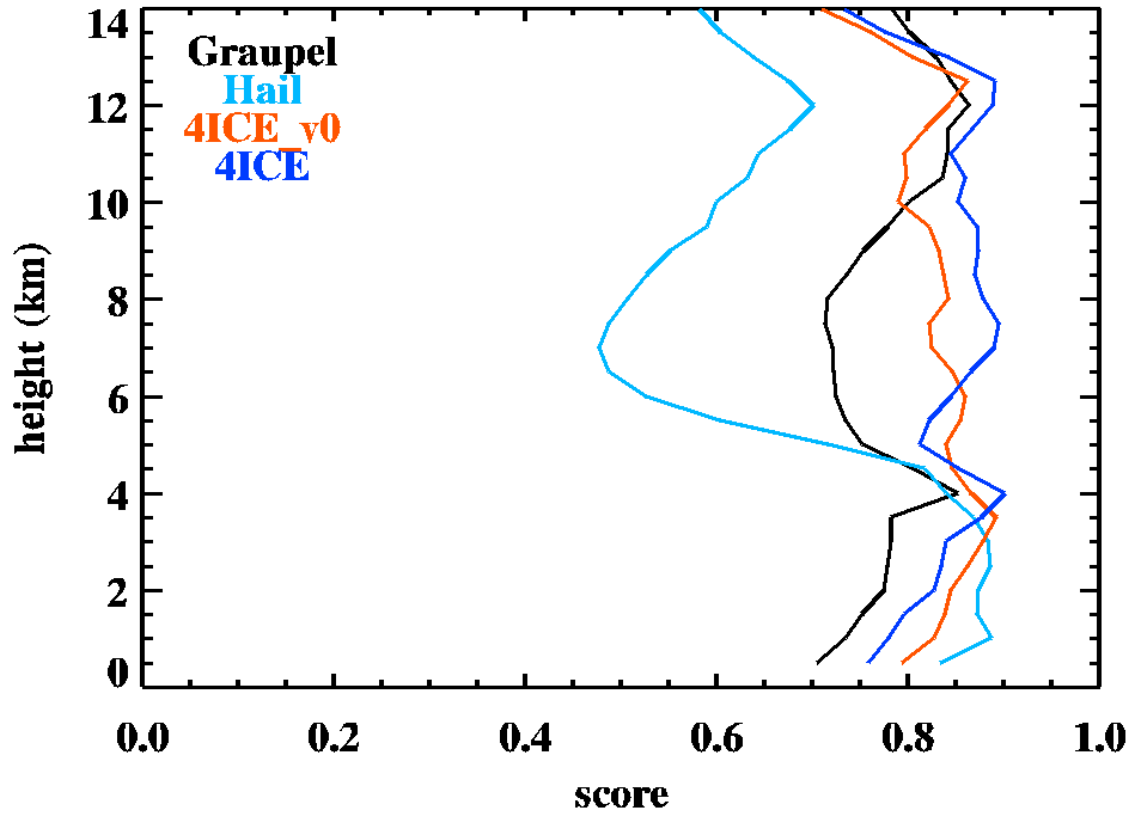
1580

1581

1582

1583

1584



1585

1586 Figure A4 Same as Figure 10 except with the previous 4ICE scheme [4ICE_v0, Lang et
1587 al., 2014] added.

1588

1589

1590

1591

1592

1593